Article
journal of Studies of Earth's Deep Interior
doi:10.46298/jsedi.16005

Constraints on the lower mantle electrical conductivity from length-of-day changes

Nicolas Gillet * [1], **Zdenek Martinec** [2,3], **Thea Lepage** [1], **Dominique Jault** [1]

[1]Univ. Grenoble Alpes, Univ. Savoie Mont Blanc, CNRS, IRD, Univ. Gustave Eiffel, ISTerre, Grenoble 38000, France, [2]Dublin Institute for Advanced Studies, School of Cosmic Physics, Geophysics Section, 5 Merrion Square, Dublin 2, Ireland, [3]Charles University, Faculty of Mathematics and Physics, Prague, Czech Republic

Author contributions: *Conceptualization*: DJ, NG, ZM. *Formal Analysis*: ZM, TL, NG. *Writing - Original draft*: NG. *Writing - Review & Editing*: NG, ZM, TL, DJ. *Project administration*: NG.

Abstract We investigate how the radial profile $\sigma_m(r)$ of the lower mantle electrical conductivity affects the downward continuation of the time-varying magnetic field to the core surface and the resulting inverted core motions. We compare core flow predictions to the length-of-day (LOD) with geodetic records, in order to assess how plausible the considered conductivity profiles are. The core flow inverse problem, mixing the information carried by single spherical harmonic magnetic coefficients, makes it non trivial to infer the delay expected for LOD predictions. Our results indicate that the timescale characteristic of the mantle filter in the low-frequency limit yields an integral measure of $\sigma_m(r)$ allowing us to select admissible conductivity models. Models of $\sigma_m(r)$ inferred from magnetospheric and tidal sources over the satellite era involve mantle filter lags less than a couple of months and provide the best fit to LOD variations. Other conductivity profiles constructed based on mineralogical properties and iron partitioning inferred for deep mantle rocks (i.e., σ_m increasing from a few S/m at 1200 km depth up to some tens of S/m ~ 300 km above the core surface, with a more conducting D" layer) are acceptable. A highly conducting layer of thickness O(10 km) or thinner cannot be excluded.

Handling Editor: Alexandre Fournier
Received: July 8, 2025
Revised: October 9, 2025; October 23, 2025
Accepted: October 31, 2025
Published: November 7, 2025

Non-technical summary The electrical conductivity σ_m of the lower mantle is poorly known, as it is difficult to investigate with electro-magnetic studies using the magnetospheric field as a source. We use instead core surface flow models inverted from magnetic observations, considering the impact of the mantle filter on the magnetic signal originating from the core. We compare predictions to length-of-day (LOD) variations from core flows with geodetic series, for various radial profiles of σ_m. The delay found between observed and predicted LOD series at decadal and interanual periods is used to assess the admissibility of the conductivity models. The best fit is found when considering σ_m as inverted from external sources. Presenting relatively larger values in the lower mantle, σ_m inferred from mineralogical properties of deep mantle rocks is still acceptable. We cannot sense this way the conductivity of a lowermost mantle layer with a thickness of some 10 km.

1 Introduction

The global geodynamics is much influenced by the presence of Large Low Velocity Provinces (LLVP) detected by seismologists (e.g. Davaille and Romanowicz, 2020). Their origin (thermal and/or chemical) remains debated, with constraints brought by high pressure mineral physics combined with seismic studies and geodynamical models (e.g. Ballmer et al., 2016; Wang et al., 2021; Talavera-Soza et al., 2025). The mantle electrical conductivity could be used as an extra constraint, since the iron content is a key ingredient for the composition of deep materials (Deschamps et al., 2012; Vilella et al., 2021). However, sounding the electrical conductivity σ_m of the mantle is restricted by the longest period of the external source variation. Using periods less than 6 months, the conductivity model is most reliably determined to the depth of ≈ 1200 km, where the conductivity reaches about 3 S/m, and the uncertainty increases rapidly at larger depths (from 1 to 30, see for instance Grayver, 2024, Fig. 13). Constraining σ_m at greater depths requires to consider longer periods, and possibly to account for more complex geometries of the external source (e.g. Grayver et al., 2021; Martinec and Velímský, 2022).

Backus (1983) developed a mantle filter theory to account for a possible association between events extracted from length-of-day (LOD) series and magnetic jerks, while Holme and Viron (2013) argued for a low electrical conductivity of the mantle as evidenced by the concomitance between jumps in LOD (interpreted as jumps in core angular momentum) and magnetic jerks. More generally, the dynamics within Earth's core may be considered to provide information about σ_m within the deep mantle. The reflection properties of torsional Alfvén waves at the core equator (Schaeffer and Jault, 2016) are sensitive to the conductance of the mantle

$$G = \int_c^a \sigma_m(r) dr \qquad (1)$$

(here restricted to a one-dimensional case with no lateral variations), with c = 3485 km the outer core radius and

*Corresponding author:
nicolas.gillet@univ-grenoble-alpes.fr

$a = 6371.2$ km the Earth's reference radius. This result may be generalized to non-axisymmetrical motions, using the boundary conditions explicited by Firsov et al. (2023). Dumberry and More (2020) explored a similar idea with a reduced model for the fluid motions in the core affected by the conductance G through electro-magnetic (EM) coupling at the core-mantle boundary (CMB). Sensing the deep mantle conductance via the core dynamics should ideally rest on a comprehensive dynamical model of the fluid core in the presence of a conducting mantle. Ultimately, simulating numerically such a dynamics in the proper parameter regime (rapid rotation, fluid viscosity much less than the magnetic diffusivity, Alfvén time-scale much longer than the day) still requires high performance computations.

Instead of a dynamical study, we consider here an alternative kinematic approach based on inverted core flows. In comparison with time-stepping a hydromagnetic model of the fluid core, it is easier to set up, and this avenue has not been fully explored yet. We are interested in the sensitivity of core surface motions, as inferred from magnetic data, to the electrical conductivity σ_m of the mantle considered for the downward continuation of the field at the Earth's surface to the bottom of the mantle. The overall goal of this study is to attest if predictions to the LOD from core motions, once confronted to geodetic observations, can be used as a criterion to obtain bounds on σ_m. Our approach differs from previous attempts conducted for instance by Holme (1998) or Gillet et al. (2015), in the sense that these were all based on field models downward continued assuming an insulating mantle.

The result of this experiment is not trivial, for several reasons. First, in the case of a thick conductive layer, the shape of the impulse response function $\gamma(t)$ characteristic of the mantle filter shall vary with the profile $\sigma_m(r)$ (e.g. Stix and Roberts, 1984; Jault, 2015). $\gamma(t)$ furthermore depends on the spherical harmonic degrees, presenting a decreasing delays for increasing degree. Finally, the core flow is related to changes in the magnetic field in a complex manner that mixes all harmonic degrees through Gaunt-Elsasser integrals (e.g. Roberts and Scott, 1965; Whaler, 1986). This complicated state of affairs motivates the empirical experiment presented in this study.

We first present in §2 how we obtain models of the radial magnetic field at the CMB in the case of a conducting mantle, and the sensitivity of the magnetic solutions at the CMB to the choice of a conductivity profile. We restrict ourselves to the case where $\sigma_m = \sigma_m(r)$ only depends on the depth (no lateral variations). Next in §3 we recall the main lines of the assimilation tool pygeodyn used to infer our flow solutions, discuss the sensitivity of the LOD prediction from inverted core flows, and analyse their delay w.r.t. the geodetic series, at both decadal and interannual timescales. Finally in §4 we conclude about bounds on the mantle electrical conductivity.

2 Magnetic solutions at the core surface for a conducting mantle

We only provide here the main lines of the reconstruction of the core surface field, knowing the magnetic field at the Earth's surface. We solve below a problem similar to that addressed by Hagedoorn and Martinec (2015), although we use here a different mathematical and numerical formulation. While in Hagedoorn and Martinec (2015) the primary variable is the toroidal magnetic potential, here it has been expressed in terms of magnetic induction vector. This change is motivated by the possible future exploration of three-dimensional induction models, although we resort here to one-dimensional models, for which the two approaches have been benchmarked to one another. A significant difference between the two approaches concerns the radial discretization, which should be significantly thinner (at least 10 times) for calculations based on the toroidal potential, in comparison with those relying on the magnetic induction vector. The full description of the method shall be provided soon in a dedicated study.

2.1 The boundary-value problem

We resort below to spherical coordinates (r, θ, ϕ). In the general case where $\sigma_m \neq 0$, the magnetic field at the core surface cannot be downward continued from surface observations as a solution of Laplace equation $\nabla^2 V = 0$. Since electrical currents flow into the mantle, $\nabla \times \boldsymbol{B} \neq 0$ and the magnetic field vector $\boldsymbol{B}$ does not derive from a potential V. Instead one has to solve a boundary value problem: we search for the magnetic field at the core surface ($r = c$), knowing the values of a potential field at the Earth's surface ($r = a$), given a profile for $\sigma_m(r)$. We then have to solve for the diffusion equation in the volume of the mantle,

$$\partial_t \boldsymbol{B} + \frac{1}{\mu} \nabla \times \left(\frac{1}{\sigma_m(r)} \nabla \times \boldsymbol{B} \right) = \boldsymbol{0}, \text{ for } c \leq r \leq a, \tag{2}$$

where μ is the magnetic permeability of free space, subject to boundary constraints. Eq.(2) represents our forward problem, for a field provided at the core surface.

We decompose the magnetic field in the mantle into its toroidal $\boldsymbol{B}_T$ and poloidal $\boldsymbol{B}_P$ components, and distinguish between the internal $\boldsymbol{B}^{(i)}$ and external $\boldsymbol{B}^{(e)}$ parts. We note $\boldsymbol{X}_H = \boldsymbol{n} \times \boldsymbol{X}$ the component of $\boldsymbol{X}$ tangential to a boundary, with $\boldsymbol{n}$ the unit vector normal to the boundary. Physically, the three components of the magnetic field have to be continuous at the Earth's surface. There, the field in the mantle attaches to a potential field external to the Earth. We restrict ourselves to a case with no currents external to the Earth. The considered boundary constraints are then:

(i) The external field vanishes above the Earth's surface:

$$\boldsymbol{B}^{(e)} = \boldsymbol{0} \text{ for } r \geq a. \tag{3}$$

(ii) The magnetic field is attached to a potential V at the Earth's surface (see §2.2), or vanishing toroidal field:

$$\boldsymbol{B}_T = \boldsymbol{0} \text{ at } r = a. \tag{4}$$

(iii) The horizontal parts $\boldsymbol{B}_H$ and $\boldsymbol{E}_H$ of the magnetic and electric fields are continuous at the Earth's surface

$$[\boldsymbol{B}_H]_{a^-}^{a^+} = [\boldsymbol{E}_H]_{a^-}^{a^+} = \boldsymbol{0} \text{ at } r = a, \tag{5}$$

where $[\boldsymbol{X}]_{a^-}^{a^+}$ denotes the jump of a vector $\boldsymbol{X}$ accross $r = a$ (assuming no surface currents and a homogeneous magnetic permeability).

(iv) A Dirichlet boundary condition applies at the core surface:

$$\boldsymbol{B}_H = \boldsymbol{B}_{|r=c}(t) \text{ at } r = c\,. \tag{6}$$

Note that $\boldsymbol{B}_{|r=c}(t)$ prescribed as the entry of the forward problem (2) is the sum of an internal field (the dynamo field from the core) and of a field external to the core, induced in the mantle.

2.2 Numerical implementation and inverse problem

The field is represented via vector spherical harmonics with a cut-off degree $N = 14$. The radial segment $[c, a]$ is subdivided into $K = 240$ finite elements. This generates a total number of $P = N(N+2)(4K+3) = 215,712$ variables for the forward problem. The term describing $\boldsymbol{B}_{|r=c}(t)$ at the bottom boundary is approximated by a projection on order 6 B-splines, with knots every 2 yr.

We prescribe the field at the surface, as inferred from magnetic data with field models, and search for the core field at the CMB using an adjoint approach (Hagedoorn and Martinec, 2015). The potential magnetic field $\boldsymbol{B}_P = -\nabla V$ for $r \geq a$ is defined via the potential

$$V(r,\theta,\phi,t) = a\sum_{n=1}^{N}\left(\frac{a}{r}\right)^{n+1}\sum_{m=0}^{n}\left(g_n^m(t)\cos(m\phi) + h_n^m(t)\sin(m\phi)\right)P_n^m(\cos\theta), \tag{7}$$

with g_n^m and h_n^m the Schmidt semi-normalized Gauss coefficients, and P_n^m the associated Legendre functions. Since we restrict ourselves to 1-dimensional conductivity profiles (see below), the solution to the boundary value problem can be sought separately for all Gauss coefficients, as they are decoupled from one another within Eq. (2).

We consider here two potential field models $\boldsymbol{B}^{obs}$ covering the XXth century as well as the satellite era, namely Kalmag (Baerenzung et al., 2022) and COV-OBS-x2 (Huder et al., 2020), over the time-span $[t_i, t_e] = [1900, 2020]$. Both models are provided as an ensemble of realizations, which allows us to provide uncertainties on the flow models, thus on the LOD predictions and their associated diagnostics: the correlation, lag and coherence w.r.t. geodetic LOD data (see §3.2). Using two different models allows us to further measure the sensitivity of our findings to the field model considered as an entry for our protocol. The two models are built using an a priori assumption on the core field from autoregressive processes of order 2, i.e. once differential main field (MF) series. Their temporal representations differ much since Kalmag is based on a sequential approach, while COV-OBS-x2 is projected onto cubic B-splines. They follow rather different modeling strategies regarding external and induced fields. COV-OBS-x2 assumes an insulating mantle, with the core responding to external dipole field variations as a perfectly conducting solid. Due to its temporal projection onto splines with 2 yr knot spacing, it is restricted to field variations longer than ≈ 3 yr. KALMAG does not account for a conductivity profile, but assumes an extra internal source a priori independent of the magnetospheric source and behaving with a restoring timescale commensurate with the day (see Table 3 in Baerenzung et al., 2022). This source accounts for both induced and ionospheric sources, which cannot be unambiguously separated given the distribution of available magnetic data. Together with their estimation of the magnetospheric field, it leads to an a posteriori estimate for an equivalent Q-response (see their Fig. 11).

The data $\boldsymbol{B}^{obs}(t)$ are smoothed by projecting onto the same B-splines as for the CMB solution we search for. This simplification is operated in order to reduce the temporal complexity, as solving for the diffusion equation (2) backward is by nature unstable. Considering knots every 2 yr still allows to describe the transient signals of period about 6 yr that are responsible for pulses in the second time-derivative of the field (e.g. Chulliat and Maus, 2014; Kloss and Finlay, 2019), and interpreted as the signature of hydro-magnetic waves in the core (Gillet et al., 2022; Gillet et al., 2024). These signals are potentially important for our purpose, as a large fraction of subdecadal oscillations detected in the LOD series (Holme and Viron, 2013; Duan and Huang, 2020; Ding et al., 2021) have been found to originate from fluid motions in the core (Istas et al., 2023; Rosat and Gillet, 2023).

Unknown parameters entering the bottom condition (6) are stored in a vector $\mathbf{p}_k$ at iteration k. The solution is sought iteratively and the distance to the data is measured via a misfit function

$$\chi^2(\mathbf{p}_k) = \frac{1}{4\pi(t_e - t_i)}\int_{t_i}^{t_e}\int_{\Sigma_a}\left[\boldsymbol{n}\times\boldsymbol{B}^{obs}(t) - \boldsymbol{n}\times\boldsymbol{B}_k(t)\right]^2\sin\theta\,\mathrm{d}\theta\mathrm{d}\phi\mathrm{d}t\,, \tag{8}$$

where Σ_a denotes the Earth's surface and $\boldsymbol{B}_k$ is the magnetic field predicted from the model parameters entering $\mathbf{p}_k$. The misfit is minimized with a conjugate gradient method, within which the model parameters $\mathbf{p}_k$ are updated. It is based on the adjoint of the misfit, calculated by an adjoint-state method. The iteration process is initialized based on $\mathbf{p}_0$ the harmonic downward continuation of surface data through an insulating mantle. Note that the solution is extended 15 years both before t_i and after t_e, in order to mitigate the impact of edges effects.

This inverse problem is not well conditioned, because the magnetic field decreases with increasing distance from its source (the core). There are many possible solutions that would match the observed field at $r = a$, just because the diffusion equation upward (propagation of the field from the CMB to the surface) tends to smooth short time-scales (e.g. Jault, 2015). We measure the complexity of the solution at the CMB at the k-th iterate through the norm of its time-derivative (or secular variation, SV)

$$L_{SV}^2(\mathbf{p}_k) = \frac{1}{4\pi(t_e - t_i)}\int_{t_i}^{t_e}\int_{\Sigma_c}\left[\boldsymbol{n}\times\frac{\partial\boldsymbol{B}_k}{\partial t}\right]^2\sin\theta\,\mathrm{d}\theta\mathrm{d}\phi\mathrm{d}t\,, \tag{9}$$

where Σ_c denotes the CMB. We show in Fig. 1 one example of trade-off curve that represents L_{SV}^2 as a function of χ^2 throughout the iterative process. The solutions considered below corresponds to the 10^{th} iterate. This choice, somewhat arbitrary, is performed to get solutions slightly rougher than what the knee of the trade-off curve would suggest, in order to avoid a too smooth model. We actually do not have access to the level of temporal complexity of the field at the CMB, which would require a dedicated study based on high performance geodynamo simulations in the presence of a conducting mantle.

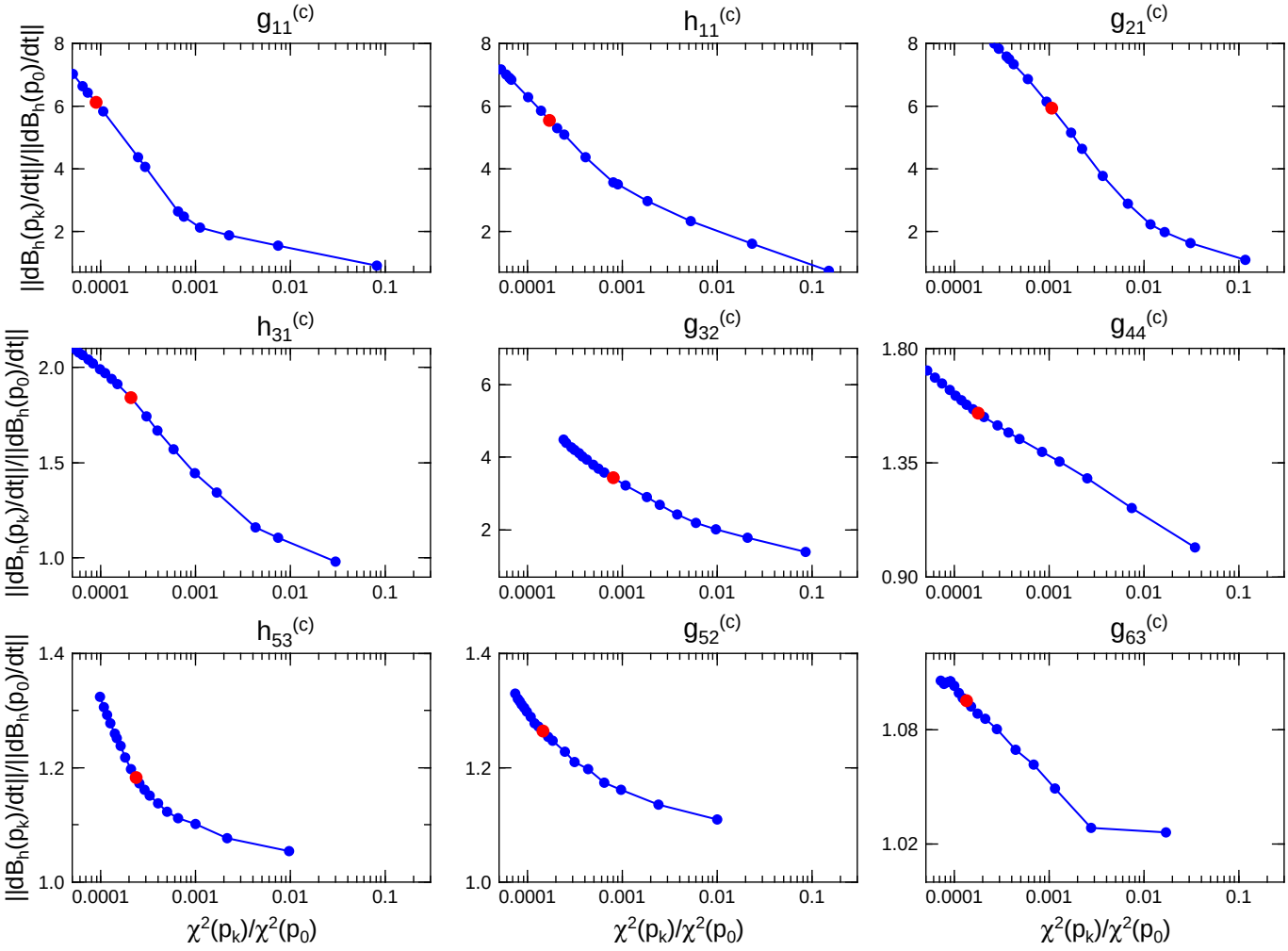

Figure 1: Trade-off curve for several Gauss coefficients in case *C*. It represents the norm L^2_{SV} as a function of the misfit χ^2 (both initialized to their initial values for $k = 0$) throughout the iterative process (from the bottom right to top left in all subplots). In red the position of the 10th iterate, chosen for the purpose of this study.

2.3 1-D conductivity profiles and associated impulse response functions

The conductance G defined by Eq. (1) is an integral quantity commonly used to measure the electrical conductivity of the mantle. However, it does not measure unambiguously how the radial distribution $\sigma_m(r)$ possibly affects the mantle filter. One may instead consider the time-scale

$$\tau_\infty = \frac{1}{2}\left(\int_c^a \sqrt{\mu\sigma(r)}\mathrm{d}r\right)^2 \tag{10}$$

derived in the high frequency approximation (Stix and Roberts, 1984), or alternatively the times

$$\tau_0(n) = \int_0^\infty t\gamma(t)\mathrm{d}t \text{ and } \tau_s(n) = \left[\int_0^\infty (t-\tau_0)^2\gamma(t)\mathrm{d}t\right]^{1/2} \tag{11}$$

introduced by Backus (1983) to describe the mantle filter in the low frequency limit. The former τ_0 measures the delay, while the latter τ_s characterizes the smoothing impact. Both decrease with the harmonic degree n. Characterizing the mantle filter via $\tau_0(n)$ is supposedly relevant when considering field changes on time-scales longer than $O(\tau_\infty)$, while this latter is appropriate on shorter periods where the penetration of magnetic variations into the mantle depends on the frequency.

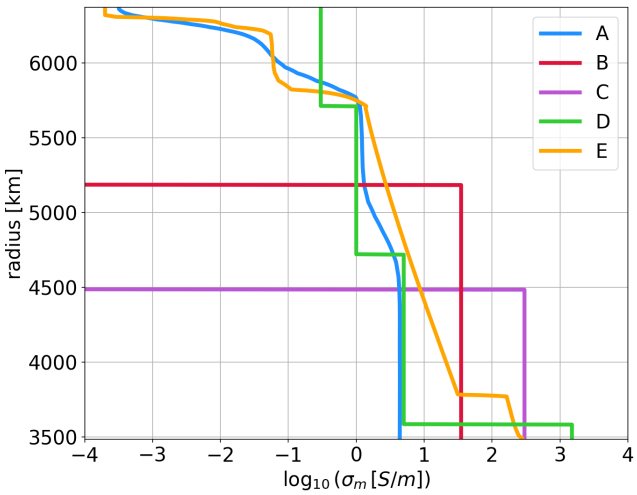

Figure 2: Radial profiles of the mantle electrical conductivity $\sigma_m(r)$ for the various cases *A* to *F* considered in this study. See text for details.

We consider here several profiles $\sigma_m(r)$, shown in Fig. 2. They correspond to conductances varying from 7×10^6 to 3×10^8 S, with either thick layers of constant conductivity (cases *B* and *C*) or a more gradual increase of the conductivity

	A	B	C	D	E
G [S]	7.1×10^6	6.0×10^7	3.0×10^8	1.6×10^8	7.7×10^7
τ_∞ [yr]	0.32	2.02	6.01	1.21	1.84
$\tau_0(n=1)$	0.28	3.88	8.20	0.59	1.59
$\tau_0(n=4)$	0.16	1.31	4.98	0.46	0.52
$\tau_0(n=7)$	0.10	0.80	3.48	0.41	0.42
$\tau_0(n=11)$	0.07	0.52	2.35	0.38	0.33
$\tau_s(n=1)$	0.22	2.93	6.62	0.55	1.23
$\tau_s(n=4)$	0.12	0.95	3.84	0.38	0.29
$\tau_s(n=7)$	0.08	0.53	2.44	0.33	0.23
$\tau_s(n=11)$	0.08	0.32	1.43	0.26	0.22

Table 1: Conductance (in S) and several characteristic timescales (in yr) for the cases A to E considered in this study. See text for details.

with depth (cases A, D and E). Model A results from an EM induction study from above, using jointly the magnetospheric Q-responses and the M_2 tidal signal, from ground-based and satellite measurements. It corresponds to the 'joint' model of Fig. 7 from Kuvshinov et al. (2021). In the deeper 1000 km of the mantle, it reaches conductivity values up to ≈ 4.5 S/m, with enhanced posterior uncertainties. Its overall conductance G_A is less than 10^7 S, and this model can be considered as a lower bound on $\sigma_m(r)$.

Alternatively we shall consider model E, which follows recent estimates of mantle electrical conductivity (see Martinec, 2025), with a conductance $G_E \simeq 7.7\times10^7$ S. The radial conductivity model by Grayver et al. (2017) defines σ_E up to the depth of 1000 km, but we know little about the conductivity of the deeper mantle. The radial dependence of σ_E, at greater depths, is tentatively estimated on the base of the thermal and composition structure of the mantle and the electrical conductivity data for the major lower mantle minerals (bridgmanite and ferropericlase). It should be noted that for both minerals, electrical conductivity has been measured, for various Fe contents, only for a limited number of high temperature and high pressure conditions, typically by holding one variable constant while varying the other. For ferropericlase we refer to Dobson and Brodholt (2000) (up to 3500 K and 32 GPa), Yoshino et al. (2011) (600 K, 53 GPa) and Ohta et al. (2014) (2100 K, 140 GPa). For bridgmanite see for instance Sinmyo et al. (2014) (along adiabatic geotherm, up to 88 GPa), Yoshino et al. (2016) (2000 K, 28 GPa), Liu et al. (2018) (300 K, 65 GPa), and Lobanov et al. (2021) (4300 K, 135 GPa). However, the available datasets remain sparse and are often restricted to specific Fe concentrations and experimental conditions, so a comprehensive systematic coverage is lacking. For this reason, we adopt the method proposed by Deschamps and Khan (2016), which relies on radially varying iron partitioning modelled using a thermodynamically consistent software framework, primarily developed by Stixrude and Lithgow-Bertelloni (2024) – we considered the red line in their Figure 12a. We modify the approach by Deschamps and Khan (2016) such that the iron partitioning in pyrolitic lower mantle follows recent results on the amount of iron, whose valence and spin state affect the electrical conductivity of the lower mantle (e.g. Xu et al., 2017; Kaminsky and Lin, 2017; Piet et al., 2016, and the references therein). The conductivity of the aggregate composed of bridgmanite and ferropericlase is estimated by the Voigt–Reuss–Hill average (Hill, 1963). Model σ_E additionally contains a high conductivity 300 km thick D" layer above the CMB according to Ohta et al. (2008).

In order to illustrate the impact of a thin and highly conductive layer at the base of the mantle, we also investigate model D, where the conductivity profile $\sigma_D(r)$ is divided in 4 layers of uniform conductivity. Introduced by Hagedoorn and Martinec (2015), it broadly summarizes the results of EM induction studies estimating $\sigma_m(r)$ based on time variations of the magnetic field of external origin. This model also considers a thin conducting layer of thickness 100 km at the bottom of the mantle where $\sigma_m = 1500$ S/m, such that $G_D \simeq 1.6\times10^8$ S. This is in agreement with some experimental estimates of the electrical conductivity for several minerals at high pressure, high temperature (transition from perovskite to post-perovskite, see Ono et al., 2006; Ohta et al., 2010).

We finally also consider two 'toy' conductivity profiles. The one of model B presents a uniform layer of thickness 1700 km and conductivity 35 S/m, so that its conductance $G_B = 6\times10^7$ S is comparable to that of model E. Both models also present similar values of τ_∞. Considering Model B will be useful to assess which of the various integral measures of $\sigma_m(r)$ is relevant for our purpose. Model C is also built in two layers of uniform conductivity. A wide layer above the CMB, of thickness 1000 km, and conductivity 300 S/m, governs its conductance $G_C = 3\times10^8$ S. We use it as an extreme case, which will clearly illustrate the impact of $\sigma_m(r)$ on both the magnetic signal and the LOD predictions.

We recall in Table 1 the conductance values of the above models, together with the values for the associated times τ_∞, τ_0 and τ_s (the latter two for several harmonic degrees). τ_∞ ranges from a few months in cases A up to 6 years in case C, presenting respectively the lowest and highest conductance values. For each considered profile $\sigma_m(r)$, $\tau_0(n)$ is comparable to $\tau_s(n)$ (actually slightly longer). For the two cases B and C presenting a thick layer of constant conductivity, τ_∞ lays between $\tau_0(1)$ and $\tau_0(4)$. Conversely, for cases A, D and E presenting a more gradual increase of $\sigma_m(r)$ with depth, $\tau_0(1)$ is shorter than τ_∞. In this respect, model B contrasts model E, despite comparable conductance values around 7×10^7 S.

We investigate below the impulse response function $\gamma(t)$ characteristic of the filter associated with the mantle conductivity profiles (leaving aside the geometric attenuation). It is calculated here for harmonic degrees $n = 1, 4, 7$ and 11 for the cases A to E, according to Section 3.2 in Jault (2015). For discontinuous models $\sigma_m(r)$, the solution $\gamma(t)$ is obtained

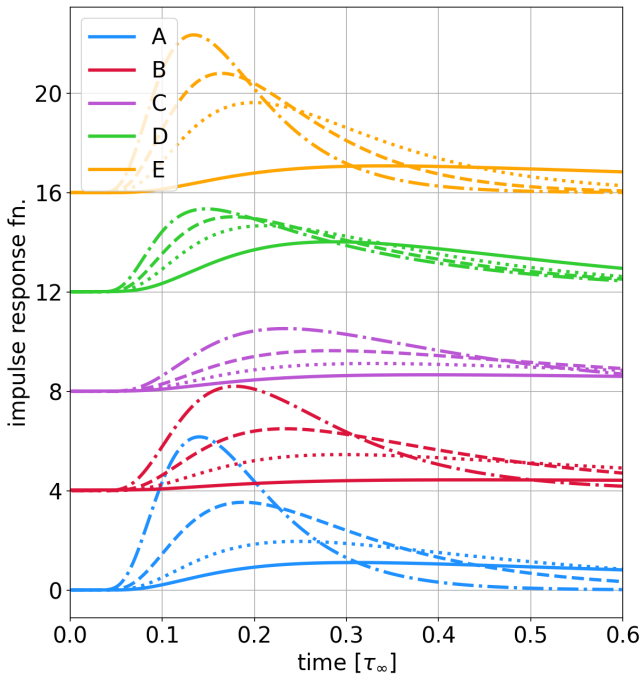

Figure 3: Impulse response functions for harmonic degrees $n = 1$ (full lines), 4 (dotted lines), 7 (dashed line) and 11 (dash-dotted), in the several cases A to E considered in this study, with time in units τ_∞. The curves have been shifted vertically to improve clarity.

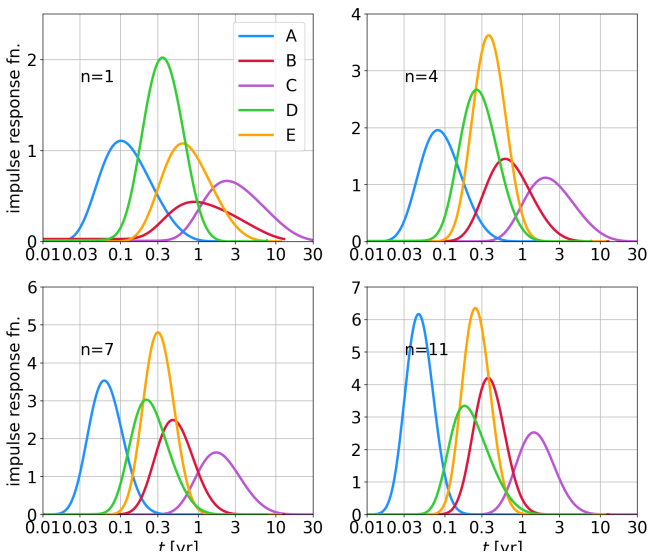

Figure 4: Impulse response functions for harmonic degrees $n = 1$ (top left), 4 (top right), 7 (bottom left) and 11 (bottom right), in the cases A to E considered in this study, with time in years and the x-axis on a log scale.

by subdividing the mantle in shells of continuous conductivity profile, then combining the solutions from all sub-layers. We first present in Fig. 3 $\gamma(t)$ with the time t in units of τ_∞. Functions have been normalized so that $\int_0^\infty \gamma(t)\mathrm{d}t = 1$. In all cases the average delay comes down to a fraction of τ_∞, and decreases with increasing harmonic degree. The shape of $\gamma(t)$ depends on the considered profile $\sigma_m(r)$. $\gamma(t)$ is relatively wider (i.e. flatter and with a longer tail) for model C with a thick uniform layer of thickness 1000 km. In comparison, the impulse response appears sharper in cases A and E. Despite presenting similar values of τ_∞, models B and E show distinct impulse response functions, which are sharper for model E. However, τ_∞ does not necessarily vary monotonically with the conductance. For instance, τ_∞ is shorter in case D than in case E despite a larger conductance, in relation with the high conductivity thin layer near the CMB in case D (see Fig. 2).

Once scaled in years, the impulse response functions are maximum at a delay spanning from some tens of days (case A) to a couple of years (case C), as illustrated in Fig. 4. The extrema in $\gamma(t)$ are of the order of a couple of months to almost one year in the intermediate cases B, D and E with a conductance around 10^8 S, depending on the model and harmonic degree n. This representation illustrates the amplitude of the expected delay in the radial SV at the core surface. Meanwhile, since functions $\gamma(t)$ expand forward with wide tails, and because the forward operator entering the core flow inverse problem mixes all length-scales, it is not trivial a priori to translate delays seen in $\gamma(t)$ into a shift between the observed and predicted LOD series. This motivates the tests performed in section 3.1.

2.4 Comparison of the downward continued secular variation and secular acceleration models

We illustrate here the impact of the choice for $\sigma_m(r)$ on the geomagnetic signal, in terms of MF, SV and secular acceleration (or SA, the second time derivative of the MF). We give in Table 2 the r.m.s. difference over the CMB between cases B to E and case A, averaged over the time span 1960–2020, for those three quantities. The starting date is chosen to focus on the era with enhanced observational constraint, following the growing number of ground observatories after the international geophysical year in 1958, and the advent of proton magnetometers (e.g. Matzka et al., 2010). Fields have been truncated to spherical harmonic degree $n = 10$, in order to mitigate the impact of the finite spatial resolution, consequence of the imperfect distribution of modern observatories (see Fig. 5 in Baerenzung et al., 2022). The comparison is performed for the COV-OBS-x2 model. We would come to similar conclusions with the Kalmag model. Because the geomagnetic field evolution is dominated by long periods, the relative changes for the MF are weak: less than 1% for cases B and E, 1.8% for case D and only up to 2.7% for case C presenting the largest conductance. All values have been normalized using the r.m.s. of case A over the same timespan. As expected, r.m.s. difference are increased when time-differentiating. For the SV it is less than 10% for cases B, D and E, but up to 26% for case C. Changes within the various flow models (and the associated LOD) inverted from various conductivity profiles will thus essentially derive from the sensitivity of the SV model at the CMB to the mantle conductivity, through the induction equation (12). R.m.s. differences are further enhanced for the SA, reaching 100% in case C. It is around 35–40% for cases B and D, and less than 30% in case E. As illustrated below, this strong impact results from the mantle filter lag and smoothing, whose effects are more visible on short periods. We recall that we do not have access to an instantaneous measure of the field changes, but rather a low-pass filtered vision of them, due to the projection on

	$A-B$	$A-C$	$A-D$	$A-E$
MF [%]	0.7	2.7	1.8	0.8
SV [%]	7.0	26.2	9.6	6.4
SA [%]	36.7	108.7	38.5	27.8

Table 2: r.m.s. of the difference between the radial component of model A and models B to E, for the MF, the SV and the SA at the CMB. Models have been truncated to spherical harmonic degree 10. Values are given in % of the r.m.s. radial MF, SV and SA for model A, and have been averaged over the timespan 1960–2020.

splines with 2 yr knot spacing. This is enough to capture the signal of period around 6 yr at the origin of SA pulses (Chulliat and Maus, 2014; Soloviev et al., 2017; Kloss and Finlay, 2019).

We show in Fig. 5 some examples of SV Gauss coefficients series obtained from COV-OBS-x2 for the various conductivity models A to E. We note $\mathrm{d}g_n^m/\mathrm{d}t$ (resp. $\mathrm{d}h_n^m/\mathrm{d}t$) the Schmidt semi-normalized SV coefficient of degree n and order m with a longitudinal phase in $\cos m\phi$ (resp. in $\sin m\phi$). These are compared with the original COV-OBS-x2 field model they derive from at $r = c$. The SV for case A (weakest conductance) almost superimposes with the original model for all harmonic degrees, as expected. The largest difference is seen for case C (strongest conductance), with a delay as large as about 5 yr for the lowermost degrees, while the interannual to decadal oscillations are amplified. The decay falls to ≈ 2 yr for $n = 7$, and becomes insignificant for degree 11 (well within the uncertainty level associated with the COV-OBS-x2 SV model). These observations are in agreement with the impulse functions from Fig. 4. Gauss coefficient series for models obtained in cases B, D and E with intermediate conductance values are at first sight close to the original field model. Nevertheless, some of the oscillations appear slightly smoothed, and for some coefficients delays up to at most 2 yr are seen for the lowermost degrees.

We present in Fig. 6 one snapshot in 1970 of the radial SV of internal origin inverted at the CMB for case A, and for the differences to cases B to E. This epochs is chosen as it is close to an intense jerk with a localized origin at the CMB (see Blangsbøll et al., 2022). The amplitude of the SV change overall increases for increasing conductances: up to $\sim 1\ \mu$T/yr for cases B, D and E, while it is as large as $\sim 3\ \mu$T/yr for case C. Changes in cases B and C (the two cases with a thick layer of uniform conductivity) present broadly similar patterns, with a decreasing magnitude from case C to B. Some of the intense patterns seen in the SV change parallel the largest patterns in the SV map for model A, with some geographical drift: Southward under the Eastern coast of North America, and under South-Africa. This is consistent with an overall backward delay of the SV with respect to case A. In some other regions, the situation is a bit more complex to decipher, as for instance under Indonesia and Australia, where we find significant changes in SV for all models whereas the SV itself is not the largest. In comparison with the thick layer cases, the geometry of the change in SV is different for models D (thin conducting layer at the bottom of the mantle) and E (gradual decrease of the conductivity from the CMB upward). In case E changes are stronger below Indonesia, South-Africa and Northern America (as for cases B and C), while in case D they are spread all over the CMB. Under Australia and South-Africa, the stronger patterns in SV change are almost anti-correlated between models (E, D) on the one side, and (B, C) on the other side. This is the consequence of the various shapes for the impulse response function as a function of the degree, obtained when varying the conductivity profile.

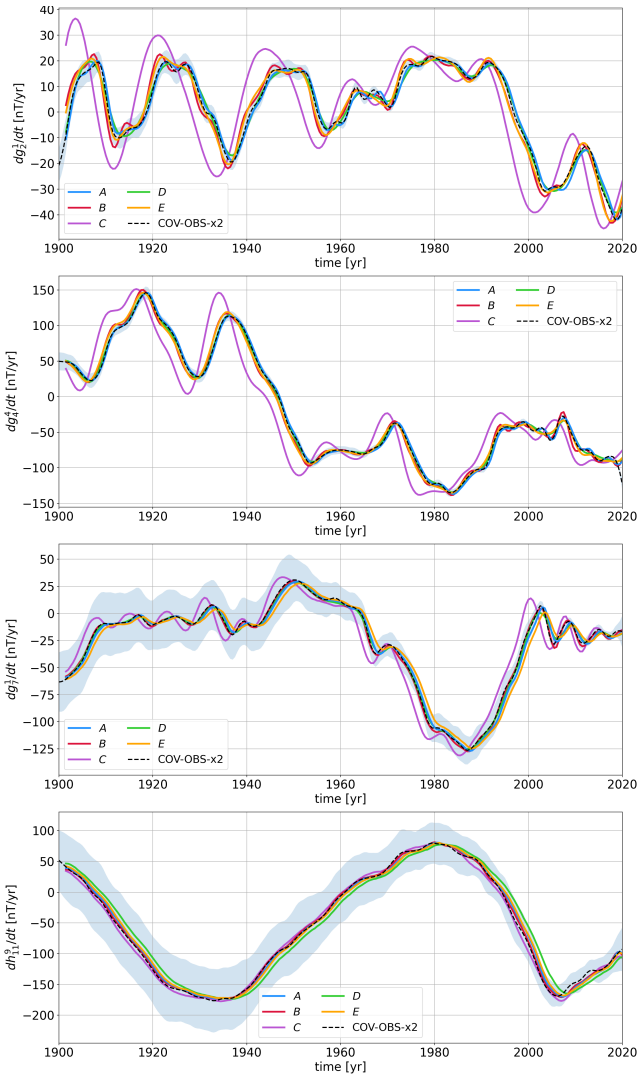

Figure 5: Some examples of SV Gauss coefficient series at the core surface for the conductivity profiles A to F considered in this study, calculated from the COV-OBS-x2 field model (in dashed black curves). Grey shaded areas indicate the uncertainties ($\pm 1\sigma$) estimated from the ensemble of SV field model coefficients.

In Fig. 7 we show the radial SA at the CMB for case A in 2016.5, period of a SA pulse, as well as the differences w.r.t. the other models. The differences w.r.t. case A present similar patterns in the two cases B and C based on two layers of uniform conductivity. The strongest features are concentrated where the SA is itself strong, for instance at low latitudes in the Western hemisphere, or at high Northern latitudes. The stronger difference is seen with cases C (the stronger considered conductance), and gives rise to $\sim 100\%$ relative error. SA differences for case E are concentrated under Central America, and are slightly weaker than in case B for comparable values of the conductance and of τ_∞. In case D, SA differences w.r.t. case A are more distributed over the CMB, as already observed for the SV, with an amplitude similar to that seen with case E. The above analysis

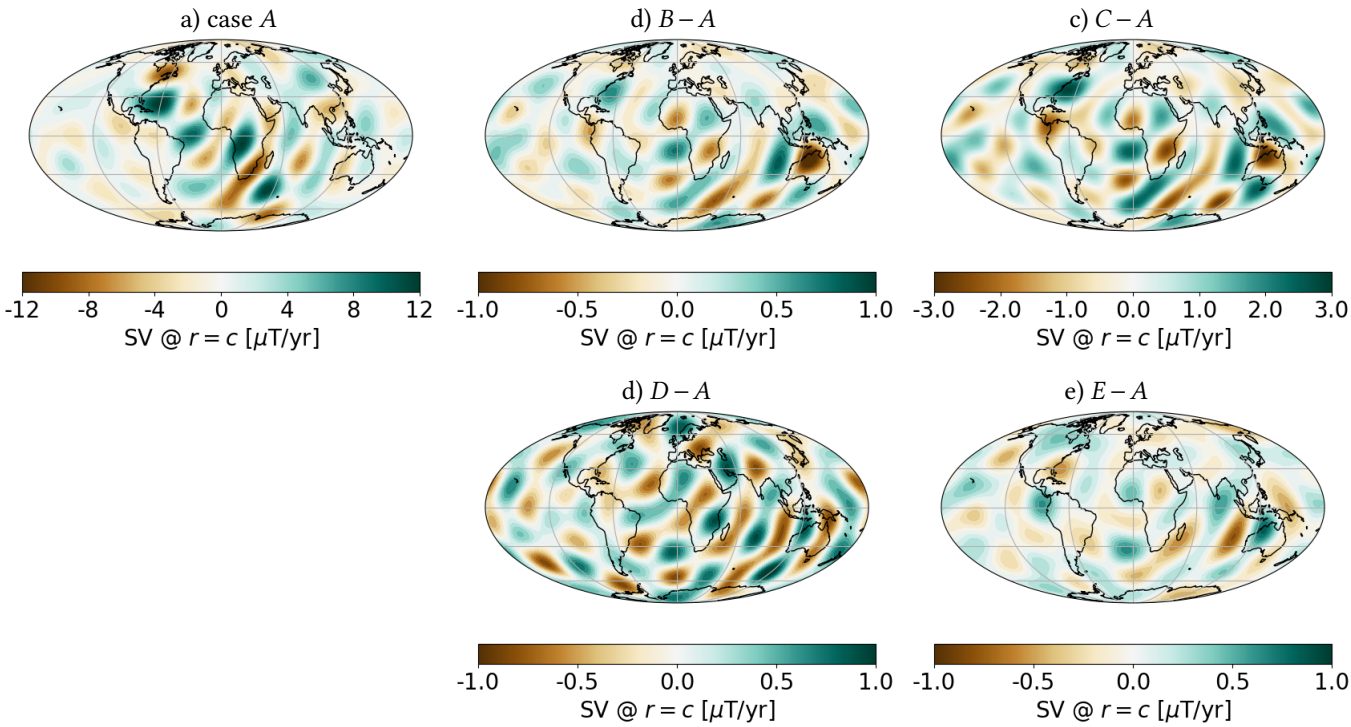

Figure 6: Radial SV $\partial_t B_r$ at the CMB inverted from COV-OBS-x2 in 1970 (in μT/yr) for the model A (a), and differences between SV maps respectively calculated for models B to E and model A (b to e). Note the different colorscales.

illustrates how the deep mantle conductivity potentially affects the morphology of transient field changes, which have been associated with major dynamical processes such as the evolution of the polar vortex (e.g. Livermore et al., 2020) or the propagation of hydromagnetic waves (Gillet et al., 2022; Grüne et al., 2025).

3 Inferred core motions and length-of-day changes when accounting for a conducting mantle

3.1 Flow estimates

For the configurations A to E listed above, we get a variety of models for the radial component $\overline{B}_r(t)$ of the dynamo magnetic field at the CMB (i.e. the internal field in $r = c$). These are restricted to the large length-scale part, as denoted by overlines, meaning here the projection on spherical harmonics of degree $n \leq N_B = 13$. We recover the horizontal core surface motions $\boldsymbol{u}_H$ by inverting the radial component of the induction equation in $r = c$,

$$\partial_t \overline{B}_r = -\overline{\nabla \cdot \left(\boldsymbol{u}_H \overline{B}_r\right)} + e_r, \tag{12}$$

using the pygeodyn tool for geomagnetic data assimilation (Huder et al., 2019). Here e_r means the errors of representativeness, that incorporate both magnetic diffusion (inaccessible from magnetic data as they require the radial derivative of $\overline{B}_r$), and the subgrid processes due to the truncation of $\boldsymbol{u}_H$ and B_r in the spectral domain (see Gillet et al., 2019). Eq. (12) is coupled to multivariate, linear, auto-regressive stochastic equations of order 1 for $\boldsymbol{u}_H$ and e_r, whose parameters are anchored to dynamo simulations (presently the *71p* dynamo of Aubert and Gillet, 2021). All fields entering the forward problem, as well as MF and SV magnetic observations, are represented with a projection onto spherical harmonics. The core surface flow is truncated at degree $N_U = 18$.

The pygeodyn tool is constructed as an augmented state ensemble Kalman filter, within which the trajectory of an ensemble of $N^e = 400$ realizations $\left\{\overline{B}_r^k, \boldsymbol{u}_H^k, e_r^k\right\}_{k\in[1,N^e]}$ is forecasted and analyzed sequentially. In our set-up, each realization for $\overline{B}_r^k(t)$ is obtained by noising the field model inverted at the CMB for a given conductivity profile. To this purpose we add for each k the difference between one realization of COV-OBS-x2 (resp. Kalmag) and the ensemble average COV-OBS-x2 (resp. Kalmag) model, as provided by Huder et al. (2020) (resp. Baerenzung et al., 2022). We use the pygeodyn version as implemented by Istas et al. (2023), where the Graphical-Lasso is considered in the empirical estimation of the forecast covariance matrix, with the parameter $\lambda_{G-Lasso} = 0.1$. The re-analysis is performed starting from 1900, with analyses performed every 6 months and a forecast time-step of 2 months.

We show in Fig. 8 some examples of zonal and non-zonal core flow coefficients. We restrict our analysis to equatorially symmetric coefficients, which dominate the flow since the model dynamics is imprinted by the quasi-geostrophic constraint inherent to the rapidly rotating geodynamo. We note ${}^c t_n^m$ (resp. ${}^s t_n^m$) the Schmidt semi-normalized toroidal flow coefficient of degree n and order m with a longitudinal phase in $\cos m\phi$ (resp. in $\sin m\phi$). Consequence of the delay observed for the lower degree SV coefficients at large conductance values, flow series are also backward shifted. For the largest considered conductance (case C), oscillations are also slightly magnified (see for instance ${}^c t_7^2$).

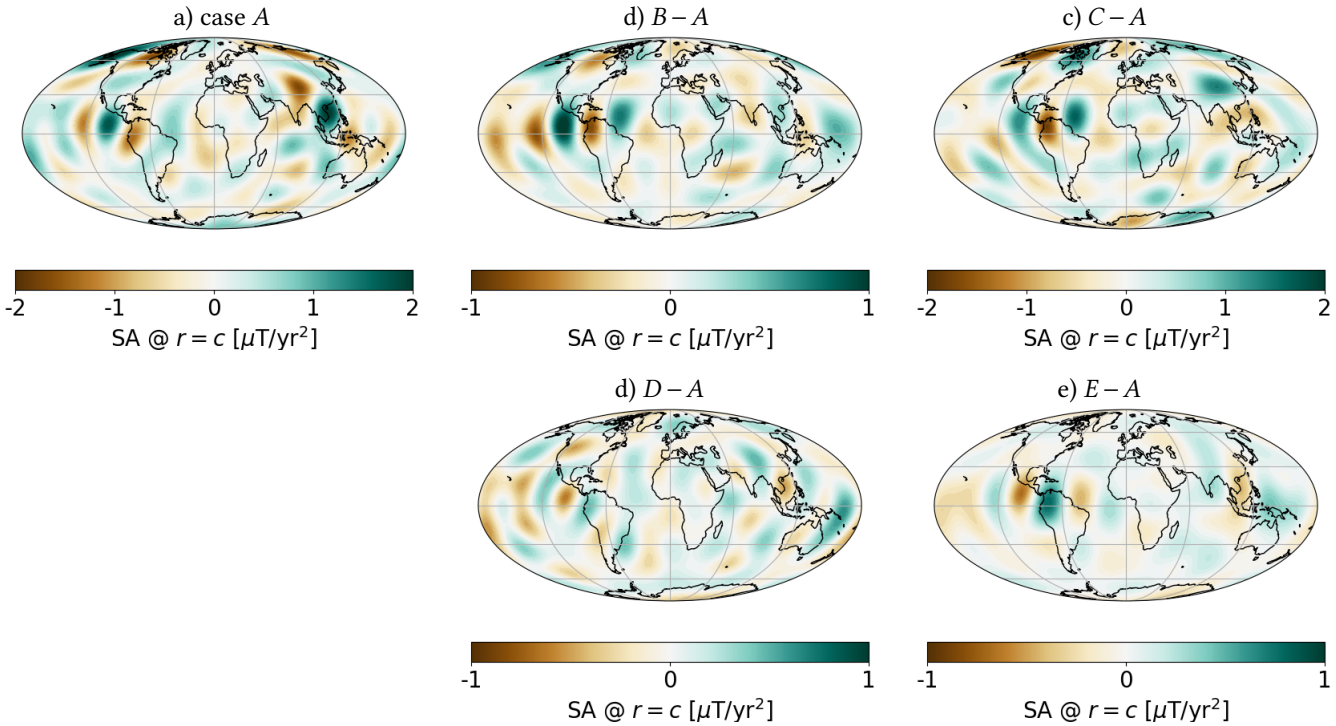

Figure 7: Radial SA $\partial^2 B_r/\partial t^2$ at the CMB inverted from COV-OBS-x2 in 2016.5 (in μT/yr^2) for the model A (a), and differences between SA maps respectively calculated for models B to E and model A (b to e). Note the different colorscales.

3.2 Length-of-day and associated diagnostics

We investigate below how the choice of conductivity profile $\sigma_m(r)$ impacts the LOD predicted from core surface flow models, and its confrontation to geodetic records. The fluid core contribution to LOD changes is estimated under the assumption that zonal motions are invariant along the rotation axis (geostrophy), assuming that the solid inner core rotates with the fluid (whose moment of inertia is in any case much smaller than that of the fluid core). In this case, the LOD prediction comes down to a linear combination of zonal flow coefficients, dominated by ${}^c t_1^0(t)$ and ${}^c t_3^0(t)$ (see Jault and Finlay, 2015, eq. 101). An evaluation of the geostrophic assumption has been carried out from one advanced geodynamo simulation (Schwaiger et al., 2024). It shows a nice agreement over a broad range of timescales, with an error of the order of 10% in magnitude for the periods considered in this study (see their Fig. 10).

LOD observations are built from the concatenation of the occultation series Lunar97 (Gross, 2001) together with the C04 series obtained from GNSS and VLBI data (Bizouard et al., 2019), once cleaned for atmospheric and tidal effects when available. Other corrections are ignored either because their estimate is tiny and uncertain (as for oceans) or because they tend to cancel each other as for land surface water and sea level (see Rosat and Gillet, 2023). A linear trend of 1.78 ms/cy has been removed to account for post-glacial rebound and tidal friction (Stephenson et al., 2016).

In the time domain we shall consider the cross-correlation function between observed and predicted LOD. Let's consider two real series $x(t)$ and $y(t)$ defined over an finite interval $[t_i, t_e]$. The cross-correlation is defined as

$$\rho(\tau) = \left[\int_{t_i}^{t_e} \tilde{x}^2(t)\mathrm{d}t \int_{t_i}^{t_e} \tilde{y}^2(t)\mathrm{d}t\right]^{-1/2} \int_{t_i}^{t_e} \tilde{x}(t)\tilde{y}(t+\tau)\mathrm{d}t\,, \quad (13)$$

where τ is the lag. We use the following convention: a negative lag between the predicted and observed LOD means that observations are ahead w.r.t. predictions (i.e. a causal mantle filter). The notation $(\tilde{x}, \tilde{y})$ denotes (x, y) once bandpass filtered within a given period range $[T_{min}, T_{max}]$ (see below). We note $\rho_0 = \rho(0)$ the zero-lag correlation, and ρ^* the maximum of the cross-correlation function. The lag that maximizes the correlation is $\tau^* = \mathrm{argmax}\{\rho(\tau)\}$, restricted to the interval where $|\tau| \leq \tau^{\max} = \sqrt{T_{min}T_{max}}/2$, in order to avoid the risk of cycle skipping.

We consider two particular period ranges, bandpass filtering the series at decadal and interannual timescales with $[T_{min}, T_{max}] = [10, 60]$ yr and $[4.5, 9.5]$ yr, respectively. We used throughout a causal Butterworth filter of order 2. We focus first on decadal periods. By using $T_{max} = (t_e - t_i)/2 = 60$ yr we avoid biasing the lag τ^* towards zero, as it would happen since we only have access to series of short duration (120 yr) in comparison with dominant pluri-decadal characteristic time-scales (see Roberts et al., 2007). In a second step we focus on interannual periods where quasi-periodic oscillations have been detected around 6 and 8.5 yr periods (Duan and Huang, 2020). This gives access to a finer temporal resolution. We exclude periods shorter than 4.5 yr where the LOD signal is dominated by atmospheric sources (Duan et al., 2015).

We will also make use of a cross-spectrum analysis. The coherence spectrum between two series $x(t)$ and $y(t)$ is expressed as

$$C_{xy}(f) = \frac{|G_{xy}(f)|^2}{|G_{xx}(f)||G_{yy}(f)|}\,, \quad (14)$$

with f the frequency. $G_{xy}(f)$ is the cross-spectral density between series x and y, and $G_{xx}(f)$ (resp. $G_{yy}(f)$) is the power spectral density (PSD) of the series x (resp. y). The coherence $C_{xy}(f)$ ranges from 0 to 1, with high values meaning

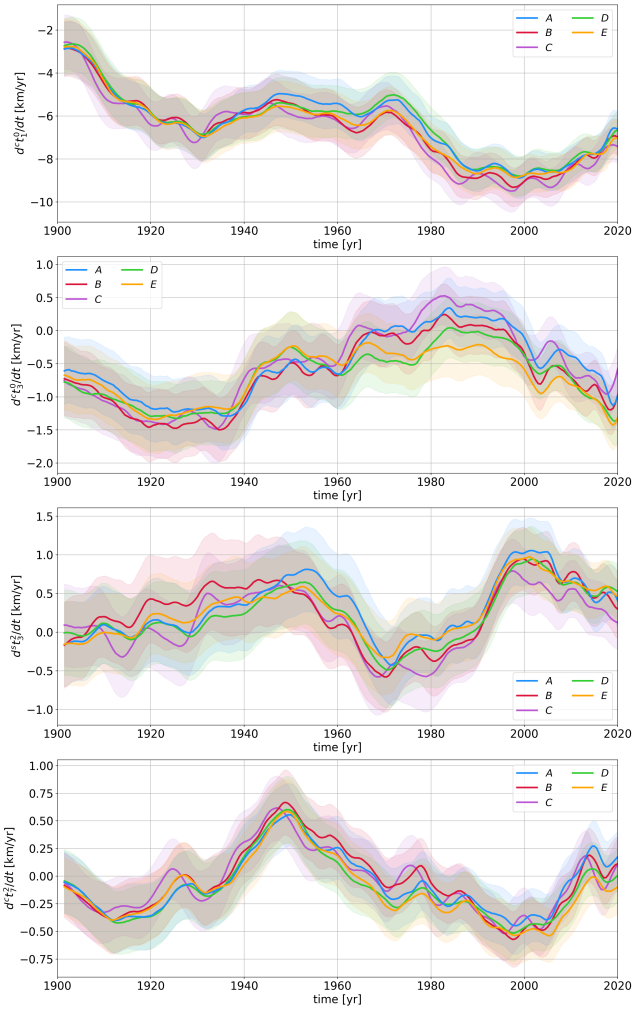

Figure 8: Some examples of core surface flow Gauss coefficient series obtained from the COV-OBS-x2 field model for the conductivity profiles A to E considered in this study. Shaded areas represent the dispersion within the ensemble of models ($\pm 1\sigma$).

that both series present a similar power. From Eq. 14 one defines the phase shift between the two series as a function of frequency, given by

$$\varphi_{xy}(f) = \arctan\left(\Im\mathrm{m}(G_{xy})/\Re\mathrm{e}(G_{xy})\right) . \qquad (15)$$

When the coherence is high, a value of φ_{xy} close to 0 means that the two signals are in phase. With our convention, a negative phase corresponds to LOD observations ahead w.r.t. predictions.

3.3 Impact of the mantle conductivity on LOD predictions

We compare in Fig. 9 geodetic LOD changes with the predicted LOD in the cases A to E, from the COV-OBS-x2 geomagnetic model. A clear shift is found for case C with the strongest conductance. It reflects the lag also found above for large scale SV and flow coefficients. This shift between LOD predictions and observations is causal, meaning that observations are ahead of predictions, because the mantle delays the signal originating from the core, and shifts the inverted flow towards the past.

In order to quantitatively assess the lag values, we calculate the cross-correlation $\rho(\tau)$ between observed and predicted series, focusing first on decadal periods $10 \leq T \leq 60$ yr.

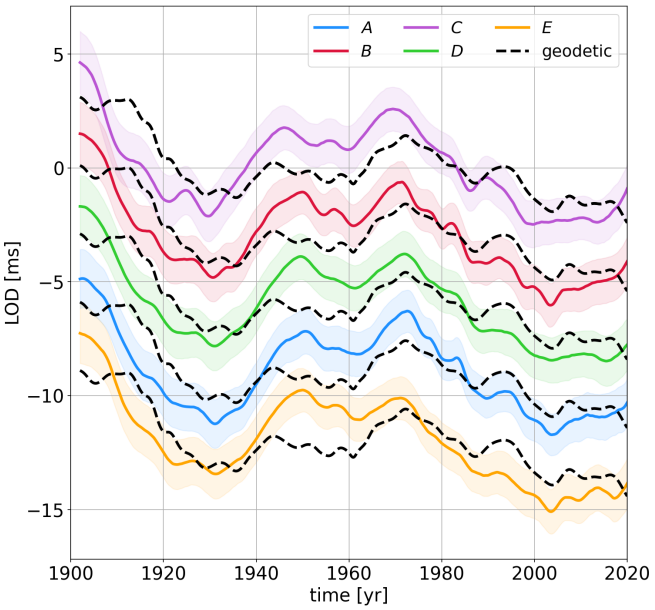

Figure 9: Predicted LOD changes for the conductivity profiles A to E, from the COV-OBS-x2 field model. Shaded areas represent the $\pm 1\sigma$ dispersion within the ensemble of models. Curves have been shifted by 3 ms from one case to the other.

This is performed both for the ensemble average model and for the ensemble of models. We report below the zero lag correlation ρ_0 and ρ^* the maximum of the cross-correlation function. The corresponding values for the ensemble mean model are denoted $\hat{\rho}_0$ and $\hat{\rho}^*$. We show in Fig. 10 histograms of ρ_0 and ρ^* from the ensemble of realizations for all conductivity models. Because correlation are bounded to 1, they present asymmetric distributions. In order to provide a comparative measure, we find it useful to fit them with the left-skewed Gumbel distribution (e.g. Coles et al., 2001)

$$p(\rho) = \frac{1}{\beta} \exp\left(\left[\frac{\rho - \overline{\rho}}{\beta}\right] - \exp\left(\left[\frac{\rho - \overline{\rho}}{\beta}\right]\right)\right) . \qquad (16)$$

This family of functions has the advantage of representing skewed asymmetric distributions. It furthermore provides a simple parameterization, relying only on two quantities: the location $\overline{\rho}$, which indicates the mode of the distribution (highest probability), and the scale β, measure of the distribution spread.

Looking at the distribution for the zero-lag correlation ρ_0, we find β within $0.10 - 0.15$ for all considered conductivity profiles. The largest value of the mode $\overline{\rho}_0 \simeq 0.61$ is found in case A (with σ_m deduced from an EM study from above, the weakest conductance), while the correlation is significantly degraded for the strongest conductance value investigated (case C), with $\overline{\rho}_0$ down to 0.50. We observed in all cases that the correlation for the ensemble mean model $\hat{\rho}_0$ is larger than the mode, with values ranging from 0.68 (case A) down to 0.54 (case C). Comparable correlations $0.60 \leq \hat{\rho}_0 \leq 0.64$ are observed for cases B, D and E, with $\overline{\rho}_0 \in [0.54, 0.58]$. For case C, the maximum ρ^* of the cross-correlation function is significantly larger than ρ_0, result of the significant lag between the observed and predicted LOD.

We show in Fig. 11 histograms for the lag τ^* for the maximum correlation within the ensemble of flow solutions, once filtered at decadal periods (10 to 60 yr). The histograms are

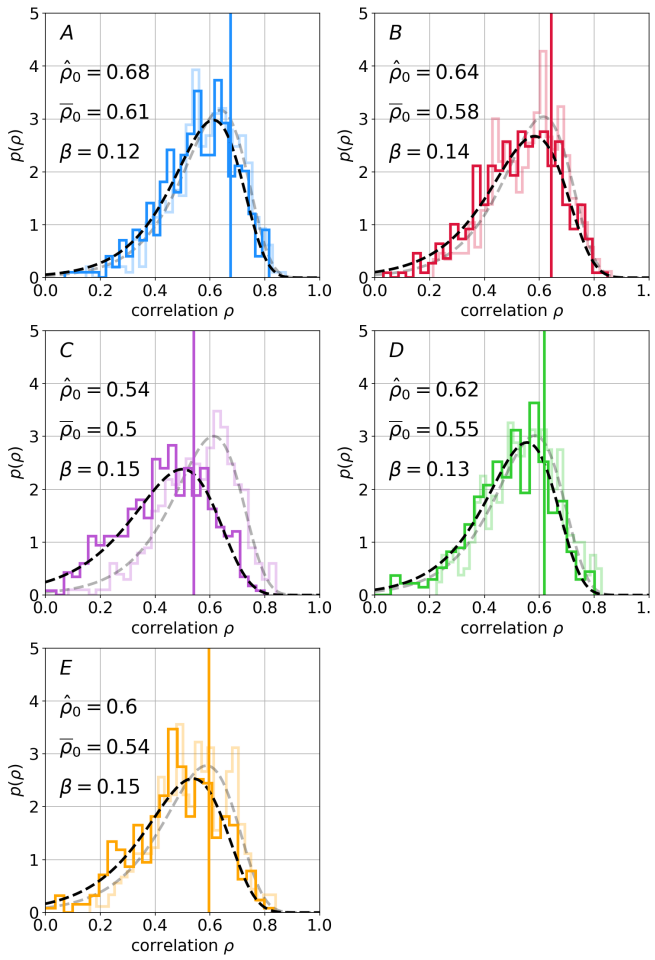

Figure 10: Histograms of the 0-lag cross-correlation ρ_0 between observed and predicted LOD series in the period range [10 – 60] yr, for the ensemble of flow models calculated based on the conductivity profiles A to E from the COV-OBS-x2 field model. The black dashed curves represent the best fit of the histograms by a left-handed Gumbel distribution with location $\overline{\rho}_0$ and scale β (see text for details). Vertical lines indicate the values of $\hat{\rho}_0$ for the ensemble mean model. In shaded color the histogram and associated fit for the maximum cross-correlation ρ^* between observed and predicted LOD series. For each distribution we indicate the mode $\overline{\rho}_0$ and scale β (see Eq. 16). Statistics have been calculated over 1900–2020.

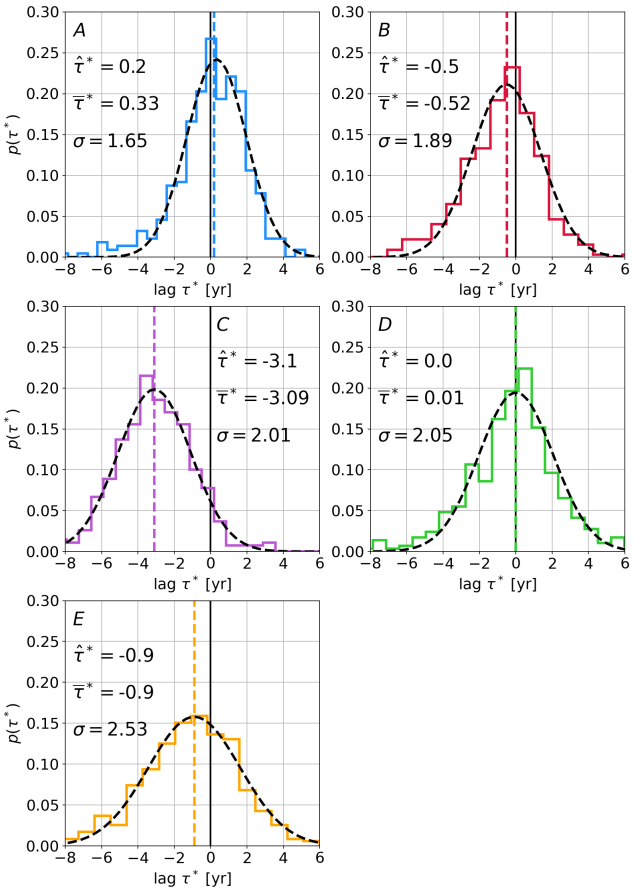

Figure 11: Histograms of the lag τ^* that maximizes the cross-correlation between observed and predicted LOD series in the period range [10 – 60] yr, within the ensemble of flow models calculated based on the conductivity profiles A to E, from the COV-OBS-x2 model. The black dashed curves represent the best fit of the histograms by a Gaussian distribution with mean μ_τ and standard deviation σ_τ (see text for details). The vertical lines indicate the values of $\hat{\tau}^*$ for the ensemble mean model. The range of acceptable lags has been restricted to $|\tau| \leq \tau^{\max} = 12.2$ yr. Statistics have been calculated over the time-span 1900–2020.

fitted with a Gaussian distribution

$$p(\tau) = \frac{1}{\sqrt{2\pi}\sigma} \exp\left(-\frac{1}{2}\left[\frac{\tau - \overline{\tau}}{\sigma}\right]^2\right), \tag{17}$$

with standard deviation σ and mean lag $\overline{\tau}$. Lag distributions within the ensemble are overall close to Gaussian, and the lag for the mean model $\hat{\tau}^*$ are close to the mean lag $\overline{\tau}^*$ in all considered cases. The spread σ in the lag is around 2 yr in all cases, from 1.65 yr in cases A up to 2.53 yr in case E. Based on this measure of the uncertainty level, the mean value $\overline{\tau} \simeq -3.1$ yr found for model C excludes a zero-lag from the $\pm 1\sigma$ interval. This model can then be excluded. All other cases A, B, D and E show a mean lag ranging within $\pm 1\sigma$: $\overline{\tau}$ is close to 0 in case A with the weakest conductance as well as in case D. Values of $\overline{\tau}$ found for cases B and E are not negative enough so that we could exclude their associated conductivity profiles based on this analysis.

In order to assess the impact of our choice of field model, we compare in Table 3 the values of $\overline{\rho}, \beta, \overline{\tau}$ and σ that characterize the distributions for the correlations and lags, as well as the corresponding values obtained for the mean model, for flow models inverted from COV-OBS-x2 and Kalmag. Zero-lag correlations (mode $\overline{\rho}_0$ and scale β for the ensemble, as well as the values for the mean models) are consistent between the two field models, with similar trends. Lag uncertainties are generally larger when using Kalmag, possibly in link with a larger short period variability due to the sequential scheme used in the construction of this model. We find for both Kalmag and COV-OBS-x2 that the ensemble mean lag is close to the lag for the mean models. Some of the lag values from Kalmag are significantly shifted backward, in comparison with COV-OBS-x2. If this effect is weak in cases A or E, it is as large as 1.7 yr in case B. Given the uncertainty values (parameter σ) this would tend to exclude, from the analysis of decadal variations, not only case C but also case B.

We now consider subdecadal periods (4.5 to 9.5 yr), focusing on the results from the COV-OBS-x2 field model. We exclude model C based on the strong lag observed at decadal time-scales. The analysis is performed starting from 1940, period over which LOD predictions from core motions have

correlation	model	A	B	C	D	E
$\overline{\rho}_0 \pm \beta$	COV-OBS-x2	0.61 ± 0.12	0.58 ± 0.14	0.50 ± 0.15	0.55 ± 0.13	0.54 ± 0.15
	Kalmag	0.57 ± 0.14	0.53 ± 0.15	0.47 ± 0.18	0.57 ± 0.13	0.53 ± 0.16
$\hat{\rho}_0$	COV-OBS-x2	0.68	0.64	0.54	0.62	0.60
	Kalmag	0.67	0.62	0.53	0.65	0.62
lag [yr]	model	A	B	C	D	E
$\overline{\tau}^* \pm \sigma$	COV-OBS-x2	0.33 ± 1.65	-0.52 ± 1.89	-3.09 ± 2.01	0.01 ± 2.05	-0.90 ± 2.53
	Kalmag	-0.27 ± 2.21	-2.27 ± 2.16	-4.36 ± 2.32	-1.43 ± 2.62	-1.19 ± 2.62
$\hat{\tau}^*$	COV-OBS-x2	0.2	-0.5	-3.1	0.0	-0.9
	Kalmag	-0.4	-2.4	-4.4	-1.6	-1.3

Table 3: Diagnostics obtained at decadal periods for the various conductivity models A to E, from the COV-OBS-x2 and Kalmag field models. Parameters $(\overline{\rho}_0, \beta)$ of the zero-lag correlation distribution within the ensemble of models, and correlation $\hat{\rho}_0$ for the ensemble mean. Parameters $(\overline{\tau}^*, \sigma)$ of the lag distribution within the ensemble of models, and lag $\hat{\tau}^*$ for the ensemble mean. See text for details.

shown a convincing fit to geodetic data even on interannual periods based on COV-OBS-x2 (Istas et al., 2023; Rosat and Gillet, 2023). The 6 yr signal in the LOD is indeed visible already from occultation observations (Madsen and Holme, 2025), prior to 1962 and the tighter constraint brought by GNSS and VLBI data. The values of $\overline{\rho}, \beta, \overline{\tau}$ and σ that characterize the distributions for the correlations and lags, as well as the corresponding values for the mean model, are summarized in Table 4. We show the histograms of lags in Fig. 12. In this period range as well the lag for the mean solution is close to the mean of the lag distribution. Conversely, the mode $\overline{\rho}_0$ of the correlation distribution is less than the correlation $\hat{\rho}_0$ for the ensemble mean. This is possibly due to the use of an AR-1 scheme for the forward model in the ensemble Kalman filter, allowing too large variability towards short periods. Cycle skipping is avoided thanks to the above analysis at decadal periods: we know that for all models (except the already excluded model C), the lag shall be less than a couple of years, leading to exclude lags larger than $\tau^{\max} \approx 3.3$ yr. Focusing on shorter periods brings a better time resolution, with σ ranging from 0.43 yr in cases B up to 1.0 yr in case D. The mean lag is well outside the $\pm 1\sigma$ range in case B, for which $|\overline{\tau}^*| > 0.8$ yr. This tends to exclude the associated conductivity model. We also note for this model (as well as for model D) a significant degradation of the zero-lag correlation $\hat{\rho}_0$ for the mean model in comparison with models A and E. None of the remaining models A, D and E, with mean lags respectively around 0.0, -0.4 and -0.6 yr, can be disregarded, even though the least conductive case seems a bit more likely.

Finally, we now compute the cross-spectrum between observed LOD and that predicted for the ensemble mean model. These diagnostics are shown in Fig. 13, performed over the time-span 1940–2020 and using as data COV-OBS-x2. The PSD for predicted and observed series show overall similar amplitudes over the considered period range. The power is nevertheless slightly reduced in case D for subdecadal periods (and to a lesser extent also in cases E and C), in comparison with geodetic observations. A relatively high coherence is found for periods above ≈ 10 yr, as well at periods around 6 yr where spectral lines have been detected (e.g. Duan and Huang, 2020; Ding et al., 2021). On periods longer than 15 yr, models D and E show the lower coherence values ($\simeq 0.5$), while it can be as large as 0.8 in case C. On interannual periods the coherence is degraded for model B (and to a lesser

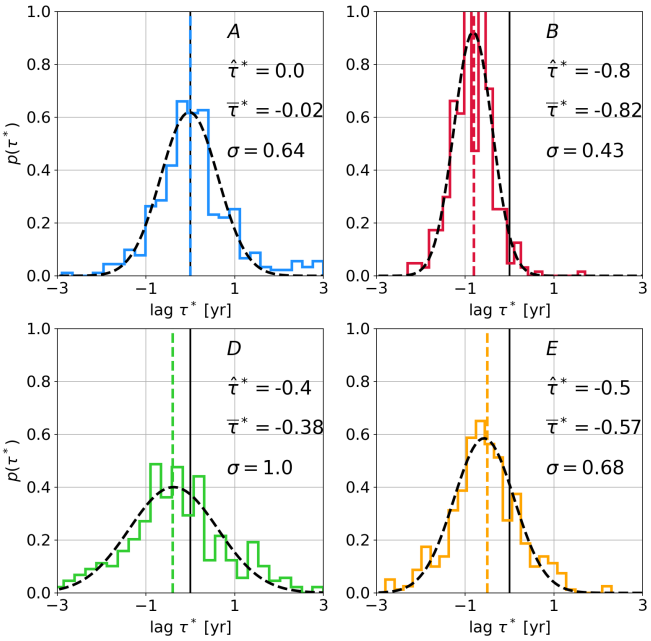

Figure 12: Same as Fig. 11 but in the period range $[4.5 - 9.5]$ yr, and for statistics calculated over the time-span 1940–2020, from the COV-OBS-x2 field model. The range of acceptable lags has been restricted to $|\tau| \leq \tau^{\max} = 3.3$ yr. Model C has been excluded based on the analysis at decadal periods.

extent D), for which the peak of large coherence shrinks. If case B shows the highest coherence on interannual periods, it is associated with a large phase lag. Significant lags are also seen in cases D and E, in line with the values given in Table 4 for the ensemble mean model. In agreement with our above analysis of the lag distributions, we notice a significant impact of the choice of conductivity profile on the phase. For periods longer than about 15 yr, while $\varphi_{xy} \lesssim 10^\circ$ for models A, B, D and E, it is shifted down to values larger than 20° in case C.

4 Summary and discussion

4.1 Bounds on the deep mantle electrical conductivity

We have downward continued the geomagnetic field from the Earth's surface to the core-mantle boundary for various

correlation	A	B	D	E
$\overline{\rho}_0 \pm \beta$	0.41 ± 0.19	0.43 ± 0.19	0.29 ± 0.22	0.39 ± 0.19
$\hat{\rho}_0$	0.72	0.62	0.60	0.69
lag [yr]	A	B	D	E
$\overline{\tau}^* \pm \sigma$	-0.02 ± 0.64	-0.82 ± 0.43	-0.38 ± 1.00	-0.57 ± 0.68
$\hat{\tau}^*$	-0.0	-0.8	-0.4	-0.5

Table 4: Diagnostics obtained at interannual periods for the various conductivity models A, B, D and E, from the COV-OBS-x2 field models. Parameters $(\overline{\rho}_0, \beta)$ of the zero-lag correlation distribution within the ensemble of models, and correlation $\hat{\rho}_0$ for the ensemble mean. Parameters $(\overline{\tau}^*, \sigma)$ of the lag distribution within the ensemble of models, and lag $\hat{\tau}^*$ for the ensemble mean. See text for details.

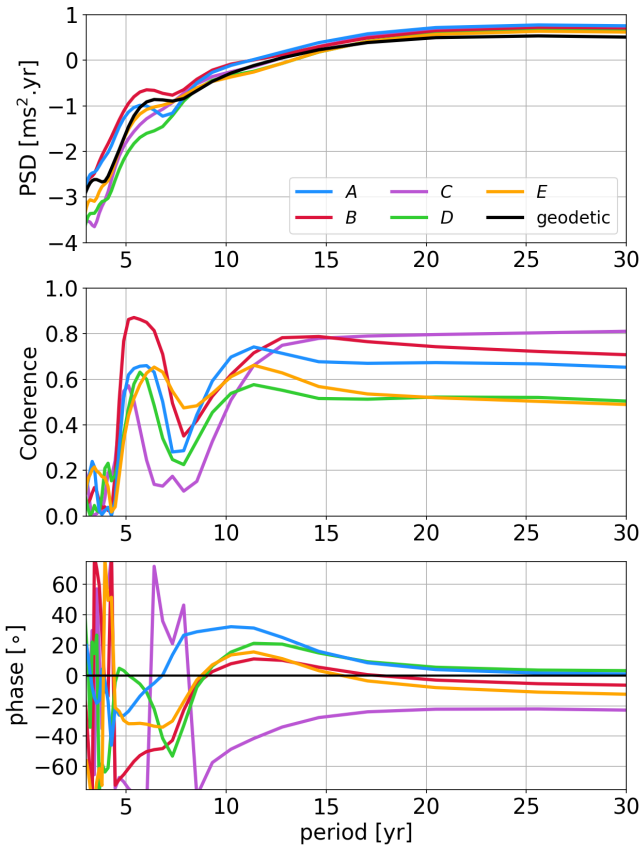

Figure 13: Top: spectral density for periods between 3 and 30 yr, for the observed and predicted LOD series from the ensemble mean model, for the several cases A to E considered in this study (from the COV-OBS-x2 field model). Middle: coherence spectrum between observed and predicted series. Bottom: associated phase lag. The analysis has been performed over the period starting from 1940, applying a Hanning window, with series zero-padded at both ends.

one-dimensional profiles $\sigma_m(r)$ of the mantle electrical conductivity, and investigated how the choice for $\sigma_m(r)$ affects the prediction from inverted core motions to the changes in the day length. The mantle filter tends to shift in time the magnetic signal, with a lag that generally increases with increasing conductances, but that also depends on the shape of the profile (thick or thin layer, gradual or abrupt changes), and varies with harmonic degree. The impact on LOD predictions was not obvious a priori, given the convolution of the magnetic signal within the core flow inverse problem. We analysed two period ranges, at decadal and interannual time-scales. The lag measured for long periods leads us to exclude conductances G as large as 3×10^8 S for a conductivity distributed over a thick layer (model C).

Considering subdecadal periods allows to refine the constraints on $\sigma_m(r)$. It shows that the conductance is not the most pertinent integral measure of the mantle conductivity, as a thick uniform layer with with $G \simeq 6 \times 10^7$ S (model B) is excluded, while model E with a gradual increase of σ_m with depth and a similar conductance, as well as model D with a larger conductance due to a thin layer at the base of the mantle, appear acceptable. The high frequency timescale τ_∞ (Stix and Roberts, 1984) cannot either be considered as a decisive measure: the thick uniform model B is excluded, contrary to model E, both presenting comparable values of τ_∞. The zero-frequency timescale τ_0 (Backus, 1983) appears as a more accurate criterion to distinguish acceptable electrical conductivity profiles. For periods longer than ~ 1 yr captured by core field models, this timescale was also favored by Jault (2015) to characterize the mantle filter. Our analysis sets an upper bound on $\tau_0(n)$ to about $\tau_0 \lesssim 1.7, 0.6$ and 0.5 yr for harmonic degrees $n = 1, 4$ and 7 respectively. We cannot exclude, based on our analysis, the presence of a ~ 10 km or thinner layer, for which the lag would become negligible.

It is worth noticing that model E constructed upon constraints from the mineralogy envisioned for deep mantle rocks appears acceptable. The fit to observed LOD changes for this model is a bit degraded in comparison with that found for profiles presenting a weaker conductivity. As such, except for the lowermost mantle to which our analysis is not sensitive, $\sigma_m(r)$ cannot be much larger than that of model E, which can then be considered as an upper bound. Seen through the prism of LOD changes and inverted core motions, the mineralogical model at the origin of the conductivity profile σ_E, with its associated model for iron partitioning, seems plausible. Meanwhile, we obtained the best scores for the weakest conductance case A where $\sigma_m(r)$ is deduced from an EM study from above (corresponding to an almost transparent mantle for our present purpose that addresses periods longer than a couple of years). This result is coherent with the diagnostics by Gillet et al. (2015) of a delay less than half a year between the observed and predicted LOD at the 6 yr period, in the case of an insulating mantle (see their Figure 11).

4.2 Perspectives regarding the deep mantle conductivity and its relation to core dynamics

Further studies are needed to account for the impact of lateral variations in $\sigma_m(r, \theta, \phi)$, which are likely present given the complex structures imaged by seismology in the deep mantle, such as LLVP. Indeed in the case of a three-dimensional

mantle conductivity, part of the poloidal field at the CMB (the observational constraint for the inference of LOD changes from core motions) enters the null space of the downward continuation from the Earth's surface: the determination of poloidal and toroidal magnetic fields at the core surface then becomes ambiguous.

The approach we have followed here is de facto restricted given its kinematic and sequential nature. To be fully consistent one would have to give up with the potential field approach and estimate the field at the CMB directly from magnetic data, provided a model of $\sigma_m(r)$. This should not affect so much the findings of the present study, as these are based on field changes operating on periods much longer than the characteristic timescale of the mantle filter. Meanwhile, the improving separation of the core and atmospheric magnetic signals give access to sharper transient field changes (Kloss et al., 2025). We may thus envision to infer core flow variations on shorter periods, where it may become necessary to account for the mantle conductivity. Alternative constraints on the mantle conductivity from core studies may arise from the temporal spectrum of the observed magnetic field. In particular we expect the core dynamics to be damped towards short timescales, because of the galvanic coupling between the core and the mantle (Firsov et al., 2023). This calls for future numerical exploration of the geodynamo in the presence of a conducting mantle, with high enough global rotation and strong enough magnetic fields for the electro-magnetic boundary conditions and the dynamics to be of geophysical interest.

4.3 Limits to the core angular momentum predictions

Estimations of LOD variations of core origin have large uncertainties. Part of this is inherent to the core flow inverse problem, which is by nature ill-posed (Backus, 1968). It is also the consequence of the important impact of subgrid processes in the observable SV at large lengthscales, and this over a broad range of periods including interannual and decadal time-scales (see Fig. 2 in Gillet et al., 2019). This effect possibly limits the improvements in LOD predictions when better observational constraint become available as with the advent of continuous global monitoring from space (Rogers et al., 2025). Kiani Shahvandi et al. (2024), who used Physics Informed Neural Networks to co-estimate the field B_r and the flow $\mathbf{u}_H$ from SV data on a grid in the physical domain, recently obtained significant albeit intriguing improvement in decadal LOD predictions over the era covered by ground-based observatories (see their figure 2b). One may wonder if this co-estimation of $\mathbf{u}_H$ and B_r on a thin grid may limit the role of subgrid processes, and if this could be the key ingredient leading to a reduction in the LOD misfit. Further such investigations are needed to assess this possibility. This promising result invites to adapt these methods for improving core-angular momentum predictions also on interannual periods.

Acknowledgements

We thank the two referees Richard Holme and Alexander Grayver whose comments helped improve the quality of our manuscript. This work has been funded by ESA in the framework of EO Science for Society, through contracts 4000127193/19/NL/IA (Swarm + 4D Deep Earth: Core) and 4000148713/25/NL/FFi (4D Earth Core+). The work on the estimation of the magnetic field at the CMB has been carried out in the framework of the project 4D Dynamic Earth funded by ESA (4000140327/23/NL/SD) as part of a EXPRO+. ZM acknowledges this support. This project was financially supported by CNES as an application of the Core_Swarm mission. NG, TL and DJ are part of Labex OSUG@2020 (ANR10 LABX56).

Data availability

- The COV-OBS-x2 model can be downloaded from http://www.spacecenter.dk/files/magnetic-models/COV-OBSx2/
- The `pygeodyn` code is available at https://gricad-gitlab.univ-grenoble-alpes.fr/Geodynamo/pygeodyn/

Competing interests

The authors have no competing interests.

References

Aubert, J. and N. Gillet (2021). The interplay of fast waves and slow convection in geodynamo simulations nearing Earth's core conditions. *Geophys. J. Int.* 225, 1854–1873. DOI: 10.1093/gji/ggab054.

Backus, G. (1968). Kinematics of geomagnetic secular variation in a perfectly conducting core. *Phil. Trans. Royal Soc. London. Series A, Mathematical and Physical Sciences* 263 (1141), 239–266. DOI: 10.1098/rsta.1968.0014.

Backus, G. E. (1983). Application of mantle filter theory to the magnetic jerk of 1969. *Geophys. J. Int.* 74 (3), 713–746. DOI: 10.1111/j.1365-246X.1983.tb01901.x.

Baerenzung, J., M. Holschneider, J. Saynisch-Wagner, and T. Maik (2022). Kalmag: a high spatio-temporal model of the geomagnetic field. *Earth, Planets and Space* 74 (1), 139. DOI: 10.1186/s40623-022-01692-5.

Ballmer, M. D., L. Schumacher, V. Lekic, C. Thomas, and G. Ito (2016). Compositional layering within the large low shear-wave velocity provinces in the lower mantle. *Geochem. Geophys. Geosyst.* 17 (12), 5056–5077. DOI: 10.1002/2016GC006605.

Bizouard, C., S. Lambert, C. Gattano, O. Becker, and J.-Y. Richard (2019). The IERS EOP 14C04 solution for Earth orientation parameters consistent with ITRF 2014. *Journal of Geodesy* 93 (5), 621–633. DOI: 10.1007/s00190-018-1186-3.

Blangsbøll, R. M., C. C. Finlay, and C. Kloss (2022). Localized Origin at the Core-Mantle Boundary of the 1969 Geomagnetic Impulse. *Geophys. Res. Lett.* 49.23, e2022GL101070. DOI: 10.1029/2022GL101070.

Chulliat, A. and S. Maus (2014). Geomagnetic secular acceleration, jerks, and a localized standing wave at the core surface from 2000 to 2010. *J. Geophys. Res.: Solid Earth* 119 (3), 1531–1543. DOI: 10.1002/2013JB010604.

Coles, S., J. Bawa, L. Trenner, and P. Dorazio (2001). An introduction to statistical modeling of extreme values. Vol. 208. Springer. DOI: 10.1007/978-1-4471-3675-0.

Davaille, A. and B. Romanowicz (2020). Deflating the LLSVPs: bundles of mantle thermochemical plumes rather than thick stagnant piles. *Tectonics* 39 (10), e2020TC006265. DOI: 10.1029/2020TC006265.

Deschamps, F. and A. Khan (2016). Electrical conductivity as a constraint on lower mantle thermo-chemical structure. *Earth Planet. Sci. Lett.* 450, 108–119. DOI: 10.1016/j.epsl.2016.06.027.

Deschamps, F., L. Cobden, and P. J. Tackley (2012). The primitive nature of large low shear-wave velocity provinces. *Earth Planet. Sci. Lett.* 349, 198–208. DOI: 10.1016/j.epsl.2012.07.012.

Ding, H., Y. An, and W. Shen (2021). New evidence for the fluctuation characteristics of intradecadal periodic signals in length-of-day variation. *J. Geophys. Res.: Solid Earth* 126 (2), e2020JB020990. DOI: 10.1029/2020JB020990.

Dobson, D. P. and J. P. Brodholt (2000). The electrical conductivity of the lower mantle phase magnesiowüstite at high temperatures and pressures. *J. Geophys. Res.: Solid Earth* 105.B1, 531–538. DOI: 10.1029/1999JB900242.

Duan, P. and C. Huang (2020). Intradecadal variations in length of day and their correspondence with geomagnetic jerks. *Nature communications* 11 (1), 1–8. DOI: 10.1038/s41467-020-16109-8.

Duan, P., G. Liu, L. Liu, X. Hu, X. Hao, Y. Huang, Z. Zhang, and B. Wang (2015). Recovery of the 6-year signal in length of day and its long-term decreasing trend. *Earth, Planets and Space* 67, 1–11. DOI: 10.1186/s40623-015-0328-6.

Dumberry, M. and C. More (2020). Weak magnetic field changes over the Pacific due to high conductance in lowermost mantle. *Nature Geoscience* 13 (7), 516–520. DOI: 10.1038/s41561-020-0589-y.

Firsov, I., D. Jault, N. Gillet, J. Aubert, and M. Mandea (2023). Radial shear in the flow at the Earth's core surface. *Geophys. J. Int.* 235 (3), 2524–2539. DOI: 10.1093/gji/ggad376.

Gillet, N., D. Jault, and C. Finlay (2015). Planetary gyre, time-dependent eddies, torsional waves, and equatorial jets at the Earth's core surface. *J. Geophys. Res.: Solid Earth* 120 (6), 3991–4013. DOI: 10.1002/2014JB011786.

Gillet, N., F. Dall'Asta, P.-O. Amblard, R. Claveau, and J. Aubert (2024). Waves in Earth's core and geomagnetic field forecast. *Phys. Earth Planet. Int.* 357, 107284. DOI: 10.1016/j.pepi.2024.107284.

Gillet, N., F. Gerick, D. Jault, T. Schwaiger, J. Aubert, and M. Istas (2022). Satellite magnetic data reveal interannual waves in Earth's core. *Proc. Nat. Acad. Sci.* 119 (13), e2115258119. DOI: 10.1073/pnas.2115258119.

Gillet, N., L. Huder, and J. Aubert (2019). A reduced stochastic model of core surface dynamics based on geodynamo simulations. *Geophys. J. Int.* 219 (1), 522–539. DOI: 10.1093/gji/ggz313.

Grayver, A. V., F. D. Munch, A. V. Kuvshinov, A. Khan, T. J. Sabaka, and L. Tøffner-Clausen (2017). Joint inversion of satellite-detected tidal and magnetospheric signals constrains electrical conductivity and water content of the upper mantle and transition zone. *Geophys. Res. Lett.* 44, 6074–6081. DOI: 10.1002/2017GL073446.

Grayver, A. (2024). Unravelling the Electrical Conductivity of Earth and Planets. *Surveys in Geophysics* 45 (1), 187–238. DOI: 10.1007/s10712-023-09813-9.

Grayver, A. V., A. Kuvshinov, and D. Werthmüller (2021). Time-Domain Modeling of Three-Dimensional Earth's and Planetary Electromagnetic Induction Effect in Ground and Satellite Observations. *J. Geophys. Res.: Space Physics* 126 (3), e2020JA028672. DOI: 10.1029/2020JA028672.

Gross, R. S. (2001). A combined length-of-day series spanning 1832–1997: LUNAR97. *Phys. Earth Planet. Int.* 123 (1), 65–76. DOI: 10.1016/S0031-9201(00)00217-X.

Grüne, C. R., K. A. Whaler, and F. D. Madsen (2025). Detecting low-latitude outer core-surface waves with 25 years of satellite secular variation data. *Phys. Earth Planet. Int.*, 107435. DOI: 10.1016/j.pepi.2025.107435.

Hagedoorn, J. and Z. Martinec (2015). The adjoint-state method for the downward continuation of the geomagnetic field. *Geophys. J. Int.* 201 (2), 724–740. DOI: 10.1093/gji/ggv049.

Hill, R. (1963). Elastic properties of reinforced solids: Some theoretical principles. *Journal of the Mechanics and Physics of Solids* 11, 357–372. DOI: 10.1016/0022-5096(63)90036-X.

Holme, R. and O. de Viron (2013). Characterization and implications of intradecadal variations in length of day. *Nature* 499, 202–204. DOI: 10.1038/nature12282.

Holme, R. (1998). Electromagnetic core-mantle coupling II: probing deep mantle conductance. *The core-mantle boundary region* 28, 139–151. DOI: 10.1029/GD028p0139.

Huder, L., N. Gillet, C. C. Finlay, M. D. Hammer, and H. Tchoungui (2020). COV-OBS.x2: 180 years of geomagnetic field evolution from ground-based and satellite observations. *Earth, Planets and Space* 72 (1), 160. DOI: 10.1186/s40623-020-01194-2.

Huder, L., N. Gillet, and F. Thollard (2019). pygeodyn 1.1. 0: a Python package for geomagnetic data assimilation. *Geosci. Model Dev.* 12 (8), 3795–3803. DOI: 10.5194/gmd-12-3795-2019.

Istas, M., N. Gillet, C. Finlay, M. Hammer, and L. Huder (2023). Transient core surface dynamics from ground and satellite geomagnetic data. *Geophys. J. Int.* 233 (3), 1890–1915. DOI: 10.1093/gji/ggad039.

Jault, D. and C. Finlay (2015). Waves in the Core and Mechanical Core–Mantle Interactions. *Treatise on Geophysics (Second Edition)*. Ed. by G. Schubert. Vol. 8. Elsevier. Chap. 8.09, pp. 225–244. DOI: 10.1016/B978-0-444-53802-4.00150-0.

Jault, D. (2015). Illuminating the electrical conductivity of the lowermost mantle from below. *Geophys. J. Int.* 202 (1), 482–496. DOI: 10.1093/gji/ggv152.

Kaminsky, F. V. and J.-F. Lin (2017). Iron partitioning in natural lower-mantle minerals: Toward a chemically heterogeneous lower mantle. *American Mineralogist* 102, 824–832. DOI: 10.2138/am-2017-5949.

Kiani Shahvandi, M., J. Noir, S. Mishra, and B. Soja (2024). Length of day variations explained in a Bayesian framework. *Geophys. Res. Lett.* 51 (22), e2024GL111148. DOI: 10.1029/2024GL111148.

Kloss, C. and C. C. Finlay (2019). Time-dependent low-latitude core flow and geomagnetic field acceleration pulses. *Geophys. J. Int.* 217 (1), 140–168. DOI: 10.1093/gji/ggy545.

Kloss, C., C. C. Finlay, N. Olsen, L. Tøffner-Clausen, N. Gillet, and A. Grayver (2025). The CHAOS-8 geomagnetic field model. *Earth, Planets and Space, under review*.

Kuvshinov, A., A. Grayver, L. Tøffner-Clausen, and N. Olsen (2021). Probing 3-D electrical conductivity of the mantle using 6 years of Swarm, CryoSat-2 and observatory magnetic data and exploiting matrix Q-responses approach.

Earth, Planets and Space 73, 67. DOI: 10.1186/s40623-020-01341-9.

Liu, J., S. M. Dorfman, F. Zhu, J. Li, Y. Wang, D. Zhang, Y. Xiao, W. Bi, and E. E. Alp (2018). Valence and spin states of iron are invisible in Earth's lower mantle. *Nature Communications* 9.1, 1284. DOI: 10.1038/s41467-018-03671-5.

Livermore, P. W., C. C. Finlay, and M. Bayliff (2020). Recent north magnetic pole acceleration towards Siberia caused by flux lobe elongation. *Nature Geoscience* 13.5, 387–391. DOI: 10.1038/s41561-020-0570-9.

Lobanov, S. S., F. Soubiran, N. Holtgrewe, J. Badro, J.-F. Lin, and A. F. Goncharov (2021). Contrasting opacity of bridgmanite and ferropericlase in the lowermost mantle: Implications to radiative and electrical conductivity. *Earth Planet. Sci. Lett.* 562, 116871. DOI: 10.1016/j.epsl.2021.116871.

Madsen, F. D. and R. Holme (2025). A recent interruption in the 6-year oscillation in length-of-day. *Geophys. J. Int.* 243.2, ggaf337. DOI: 10.1093/gji/ggaf337.

Martinec, Z. (2025). Iterative downward continuation of the geomagnetic field through a three-dimensional conducting mantle. *Geophys. J. Int.* 243 (3), ggaf380. DOI: 10.1093/gji/ggaf380.

Martinec, Z. and J. Velímský (2022). An electric circuit model of the Earth's polar electrojets and field-aligned currents for the estimation of magnetospheric magnetic field from along-track Swarm magnetic data. *Earth, Planets and Space* 74.1, 157. DOI: 10.1186/s40623-022-01716-0.

Matzka, J., A. Chulliat, M. Mandea, C. C. Finlay, and E. Qamili (2010). Geomagnetic observations for main field studies: from ground to space. *Space science reviews* 155, 29–64. DOI: 10.1007/s11214-010-9693-4.

Ohta, K., K. Fujino, Y. Kuwayama, T. Kondo, K. Shimizu, and Y. Ohishi (2014). Highly conductive iron-rich (Mg, Fe) O magnesiowüstite and its stability in the Earth's lower mantle. *J. Geophys. Res.: Solid Earth* 119.6, 4656–4665. DOI: 10.1002/2014JB010972.

Ohta, K., S. Onoda, H. Hirose, R. Sinmyo, K. Shimizu, N. Sata, Y. Ohishi, and A. Yasuhara (2008). The electrical conductivity of post-perovskite in Earth's D" layer. *Science* 320, 89–91. DOI: 10.1126/science.1155148.

Ohta, K., K. Hirose, M. Ichiki, K. Shimizu, N. Sata, and Y. Ohishi (2010). Electrical conductivities of pyrolitic mantle and MORB materials up to the lowermost mantle conditions. *Earth Planet. Sci. Lett.* 289 (3-4), 497–502. DOI: 10.1016/j.epsl.2009.11.042.

Ono, S., A. R. Oganov, T. Koyama, and H. Shimizu (2006). Stability and compressibility of the high-pressure phases of Al2O3 up to 200 GPa: Implications for the electrical conductivity of the base of the lower mantle. *Earth Planet. Sci. Lett.* 246 (3-4), 326–335. DOI: 10.1016/j.epsl.2006.04.017.

Piet, H., J. Badro, F. Nabiei, T. Dennenwaldt, S. Shim, M. Cantoni, C. Hébert, and P. Gillet (2016). Spin and valence dependence of iron partitioning in Earth's deep mantle. *Proc. Natl. Acad. Sci. U.S.A.* 113, 11127–11130. DOI: 10.1073/pnas.1605290113.

Roberts, P. and S. Scott (1965). On analysis of the secular variation 1. A hydromagnetic constraint: theory. *J geomag. geoelec.* 17 (2), 137–151. DOI: 10.5636/jgg.17.137.

Roberts, P., Z. Yu, and C. Russell (2007). On the 60-year signal from the core. *Geophys. Astrophys. Fluid Dyn.* 101 (1), 11–35. DOI: 10.1080/03091920601083820.

Rogers, H. F., N. Gillet, J. Aubert, P. Personnettaz, and M. Mandea (2025). Effects of geodynamo priors and geomagnetic data on inverted core surface flows. *Phys. Earth Planet. Int.* 364, 107323. DOI: 10.1016/j.pepi.2025.107323.

Rosat, S. and N. Gillet (2023). Intradecadal variations in length of day: Coherence with models of the Earth's core dynamics. *Phys. Earth Planet. Int.* 341, 107053. DOI: 10.1016/j.pepi.2023.107053.

Schaeffer, N. and D. Jault (2016). Electrical conductivity of the lowermost mantle explains absorption of core torsional waves at the equator. *Geophys. Res. Lett.* 43 (10), 4922–4928. DOI: 10.1002/2016GL068301.

Schwaiger, T., N. Gillet, D. Jault, M. Istas, and M. Mandea (2024). Wave-like motions and torques in Earth's core as inferred from geomagnetic data: A synthetic study. *Phys. Earth Planet. Int.* 346, 107104. DOI: 10.1016/j.pepi.2023.107104.

Sinmyo, R., G. Pesce, E. Greenberg, C. McCammon, and L. Dubrovinsky (2014). Lower mantle electrical conductivity based on measurements of Al, Fe-bearing perovskite under lower mantle conditions. *Earth Planet. Sci. Lett.* 393, 165–172. DOI: 10.1016/j.epsl.2014.02.049.

Soloviev, A., A. Chulliat, and S. Bogoutdinov (2017). Detection of secular acceleration pulses from magnetic observatory data. *Phys. Earth Planet. Int.* 270, 128–142. DOI: 10.1016/j.pepi.2017.07.005.

Stephenson, F., L. Morrison, and C. Hohenkerk (2016). Measurement of the Earth's rotation: 720 BC to AD 2015. *Proc. R. Soc. A* 472 (2196), 20160404. DOI: 10.1098/rspa.2016.0404.

Stix, M. and P. Roberts (1984). Time-dependent electromagnetic core-mantle coupling. *Phys. Earth Planet. Int.* 36 (1), 49–60. DOI: 10.1016/0031-9201(84)90098-0.

Stixrude, L. and C. Lithgow-Bertelloni (2024). Thermodynamics of mantle minerals - III: the role of iron. *Geophys. J. Int.* 237, 1699–1733. DOI: 10.1093/gji/ggae126.

Talavera-Soza, S., L. Cobden, U. H. Faul, and A. Deuss (2025). Global 3D model of mantle attenuation using seismic normal modes. *Nature* 637, 1131–1135. DOI: 10.1038/s41586-024-08322-y.

Vilella, K., T. Bodin, C.-E. Boukaré, F. Deschamps, J. Badro, M. D. Ballmer, and Y. Li (2021). Constraints on the composition and temperature of LLSVPs from seismic properties of lower mantle minerals. *Earth Planet. Sci. Lett.* 554, 116685. DOI: 10.1016/j.epsl.2020.116685.

Wang, W., J. Liu, F. Zhu, M. Li, S. M. Dorfman, J. Li, and Z. Wu (2021). Formation of large low shear velocity provinces through the decomposition of oxidized mantle. *Nature comm.* 12 (1), 1911. DOI: 10.1038/s41467-021-22185-1.

Whaler, K. (1986). Geomagnetic evidence for fluid upwelling at the core-mantle boundary. *Geophys. J. Int.* 86 (2), 563–588. DOI: 10.1111/j.1365-246X.1986.tb03844.x.

Xu, S., J.-F. Lin, and D. Morgan (2017). Iron partitioning between ferropericlase and bridgmanite in the Earth's lower mantle. *J. Geophys. Res., Solid Earth* 122, 1074–1087. DOI: 10.1002/2016JB013543.

Yoshino, T., E. Ito, T. Katsura, D. Yamazaki, S. Shan, X. Guo, M. Nishi, Y. Higo, and K.-i. Funakoshi (2011). Effect of iron content on electrical conductivity of ferropericlase with implications for the spin transition pressure. *J. Geophys. Res.: Solid Earth* 116.B4. DOI: 10.1029/2010JB007801.

Yoshino, T., S. Kamada, C. Zhao, E. Ohtani, and N. Hirao (2016). Electrical conductivity model of Al-bearing bridg-

manite with implications for the electrical structure of the Earth's lower mantle. *Earth Planet. Sci. Lett.* 434, 208–219. DOI: 10.1016/j.epsl.2015.11.032.